Theses and Dissertations

2004-12-03

Wave Scattering From Infinite Cylindrical Obstacles of Arbitrary Cross-Section

Matthew B. Weber
Brigham Young University - Provo

Follow this and additional works at: https://scholarsarchive.byu.edu/etd

Part of the Mathematics Commons

www.manaraa.com

WAVE SCATTERING FROM INFINITE CYLINDRICAL OBSTACLES

OF ARBITRARY CROSS-SECTION

by

Matthew B. Weber

A thesis submitted to the faculty of

Brigham Young University

in partial fulfillment of the requirements for the degree of

Master of Science

Department of Mathematics

Brigham Young University

November 2004

BRIGHAM YOUNG UNIVERSITY

GRADUATE COMMITTEE APPROVAL

of a thesis submitted by

Matthew B. Weber

This thesis has been read by each member of the following graduate committee and by majority vote has been found to be satisfactory.

_____	_____
Date	Vianey Villamizar, Chair
_____	_____
Date	Kening Lu
_____	_____
Date	Sum Chow

BRIGHAM YOUNG UNIVERSITY

As chair of the candidate's graduate committee, I have read the thesis of Matthew B. Weber in its final form and have found that (1) its format, citations, and bibliographical style are consistent and acceptable and fulfill university and department style requirements; (2) its illustrative materials including figures, tables, and charts are in place; and (3) the final manuscript is satisfactory to the graduate committee and is ready for submission to the university library.

_____   _____
Date   Vianey Villamizar
                                 Chair, Graduate Committee

Accepted for the Department   _____
                                 Tyler Jarvis
                                 Graduate Coordinator

Accepted for the College   _____
                                 G. Rex Bryce, Associate Dean
                                 College of Physical and Mathematical Sciences

ABSTRACT

WAVE SCATTERING FROM INFINITE CYLINDRICAL OBSTACLES
OF ARBITRARY CROSS-SECTION

Matthew B. Weber

Department of Mathematics

Master of Science

In this work the scattering of an incident plane wave propagating along a plane perpendicular to the $xy-$plane is studied. The wave is scattered from an infinitely long cylindrical object of arbitrary cross-section. Due to the arbitrary geometry of the obstacle, a finite differences numerical method is employed to approximate the solution of the scattering problems. The wave equation is expressed in terms of generalized curvilinear coordinates. Boundary conforming grids are generated using elliptic grid generators. Then, a explicit marching in time scheme is implemented over these grids. It is found that as time grows the numerical solution converges to a wave with harmonic time dependence. The amplitude of these waves is analyzed and graphed over generalized grids for different geometries. An important physical measure of the energy scattered, the differential scattering cross section, is also obtained. In particular, the method is applied to a circular cylindrical obstacle. For this case, the analytical solution can also be obtained by traditional spectral techniques. The method is validated by comparing this exact solution with the numerical approximation obtained from the application of it.

Contents

List of Figures

1 Introduction

Wave scattering emerges in many contexts. For example, from a receiving antenna in an electromagnetic field [6], when a sound pressure wave finds an obstacle in an unbounded medium, or when an elastic wave propagating underground hits a crack saturated by oil in sedimentary rocks [7]. It is easy to prove how the wave equation models all these wave scattering phenomena that arise in such seemingly unrelated fields. In general, analytic solutions for wave scattering problems are not possible to obtain. This is the case when the scatter has an arbitrary shape. That's why numerical methods are commonly used in wave scattering. Our work is based on finite differences time-domain numerical methods to approximate the solution of wave scattering problems. The application of this technique requires appropriate definition of radiation conditions at artificial boundaries at infinity, the construction of boundary-conforming coordinates when the obstacle is of arbitrary shape, and the reformulation of the boundary value problem (BVP) in terms of the new curvilinear coordinates. All these aspects are included in this study. Our focus in this work is
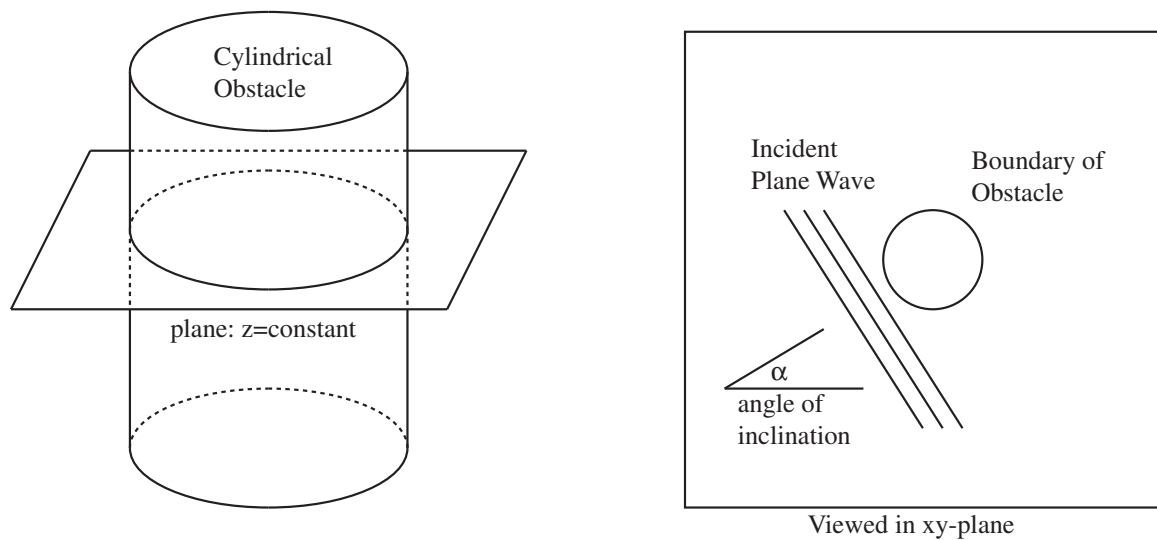
Figure 1: A cross-section of the obstacle perpendicular to the z-axis which shows the angle of inclination ρ of the incident wave

1

in the scattering of an incident plane wave propagating along a plane perpendicular to the $xy-$plane. The wave is scattered from an infinitely long cylindrical object of arbitrary cross-section. Because of the nature of the object and the trajectory of the incoming wave, the mathematical model for the problem can be reduced to a two-dimensional physical domain as seen in Fig. (1). This allows a study of the dispersion of the wave by the region traced by the object in the $xy-$plane. The results hold for any horizontal cross section of the object determined by an arbitrary plane $z=$constant.

Analytic solutions can only be obtained for very simple geometries where it is easy to compute the corresponding eigenfunctions, or the Green's function. Therefore, solutions of problems with obstacles of arbitrary shape need to be approximated numerically. Most numerical work is performed over rectangular grids combined with some kind of interpolation near the boundaries. A very popular method is for example, the use of rectangular coordinates with a stair-cased approximation at the boundaries [8]. In some cases, the interpolation at the boundaries may lead to important errors in the numerical computation. For this reason, we adopt a global definition of the grid. It means that a boundary conforming grid is generated without using interpolation. More precisely, a transformation from a rectangular coordinate system in variables ξ and η to a coordinate system conforming to the boundary of the region traced by the object in the $xy-$plane is devised. This is done by defining an initial transformation, $\mathcal{T}' : \mathcal{D}' \to \mathcal{D}$, from a rectangular computational grid, $\mathcal{D}'$, to a boundary-defined multiply connected physical region, $\mathcal{D}$. Using grid generation methods the initial grid is conformed to the boundaries of the region resulting in a smooth transformation

$$\mathcal{T} : \mathcal{D}' \to \mathcal{D}$$

$$\mathcal{T} : (\xi, \eta) \mapsto (x, y)$$

2

where $x = x(\xi, \eta)$ and $y = y(\xi, \eta)$. The result is a differentiable transformation that is injective apart from the branch cut. The initial boundary value problem governing the dispersion of the wave is solved on the physical region, $\mathcal{D}$.

As a first step we study the initial boundary value problem (IBVP) which models the dispersion of an incident plane wave by a circular cylindrical obstacle. It serves as the foundation for determining the accuracy for the results we will later obtain for non-circular cylindrical obstacles. The wave equation defined over a circular geometry is separable in polar coordinates. Therefore, analytical solutions for the IBVP can be easily obtained. A finite-differences numerical approximation using polar coordinates can also be easily obtained. The polar transformation

$$\mathcal{T} : \mathcal{D}' \to \mathcal{D}$$
$$\mathcal{T} : (r, \theta) \mapsto (x, y)$$

where $x = r \cos \theta$ and $y = r \sin \theta$. The polar transformation is boundary conforming, smooth, and injective but is only useful for the circular region. Three decades ago Thompson and others [9] popularized a way to generate boundary conforming grids by numerically solving a BVP governed by a system of elliptic partial differential equations. The unknown functions of this system are precisely the new curvilinear coordinates sought. This technique was first introduced by Winslow [5] and we will call it Winslow's grid generator (WGN). In this study, we define the coordinates transformation as the numerical solution obtained from the WGN. The resulting grid is boundary conforming, injective, and smooth. For an arbitrary region it is necessary to devise a different transformation, one that is also injective and smooth. Winslow's grid generator is a method which gives such a boundary conforming transformation. The accuracy of the numerical solutions to the IBVP using a Winslow grid is determined by comparing these solutions for the circular region to the known analytical

3

solution. This serves as a basis for inferring the accuracy of the solutions for the arbitrarily shaped regions.

2   Scattered Wave problem for a Cylindrical Obstacle with Circular Cross-Section

For acoustic problems, under the hypothesis of small disturbance from an equilibrium state, the leading order pressure term p satisfies the wave equation

$$p_{tt}(x, y, t) = c^2 \nabla^2 p(x, y, t) \tag{1}$$

where $c = w/k$. We will assume that there is an incident wave propagating in a direction parallel to the xy-plane at an angle of inclination ρ from the x-axis. If the axis of the cylindrical obstacle is the z-axis, then the scattered wave is the same in every plane $z =$constant. Therefore the problem reduces to only two spacial dimensions as can be seen in Fig. (1).

For a circular cylinder it is convenient to use polar coordinates. The change from cartesian to polar coordinates can be seen as a transformation

$$\mathcal{T} : [0, r_\infty) \times [0, 2\pi) \rightarrow \mathbb{R}^2$$
$$\mathcal{T} : (r, \theta) \mapsto \Big(x(r, \theta), y(r, \theta) \Big),$$

which transformation is depicted in Fig. (2). The incident wave is defined as

$$p_{inc}(x, y, t) = e^{ik(x \cos \rho + y \sin \rho)} e^{-iwt}, \tag{2}$$

4
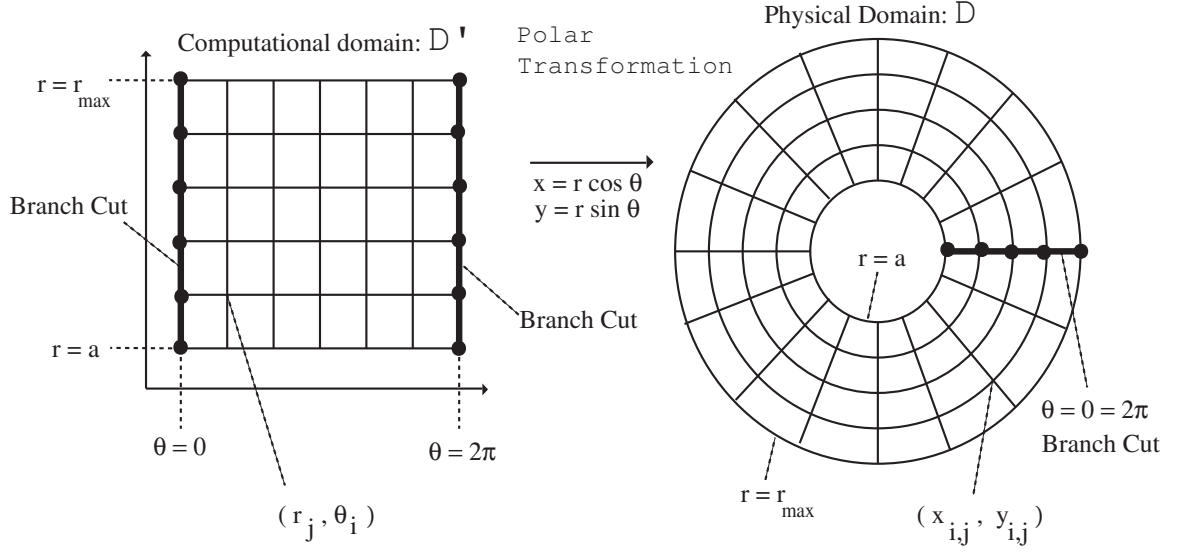
Figure 2: The Polar transformation from a computational domain $\mathcal{D}'$ to a multiply connected physical domain $\mathcal{D}$

which in polar coordinates reduces to

$$p_{inc}(r, \theta, t) = e^{ikr \cos(\theta - \rho)} e^{-iwt} = \bar{p}_{inc}(r, \theta) e^{-iwt}. \tag{3}$$

We will assume a soft cylindrical obstacle. Then, the condition at the boundary of the obstacle $(r = a)$ is given by

$$p(a, \theta, t) = 0. \tag{4}$$

The scattered pressure, p_{sc}, is defined as the difference

$$p_{sc}(r, \theta, t) = p(r, \theta, t) - p_{inc}(r, \theta, t). \tag{5}$$

It can easily be shown that the incident wave p_{inc} satisfies equation (1), then the scattered pressure p_{sc} should also satisfy equation (1). The boundary condition (4)

5

in terms of p_{sc} transforms into

$$p_{sc}(a,\theta,t) = -p_{inc}(a,\theta,t) = -\bar{p}_{inc}(a,\theta)e^{-iwt} = -e^{ika\cos(\theta-\rho)}e^{-iwt} \qquad (6)$$

For the problem to be well posed we need to impose a condition at r_∞ for the scattered pressure p_{sc}. The well-known radiation condition due to Sommerfeld is given by

$$(p_{sc})_t + c(p_{sc})_r \to 0 \text{ as } r \to \infty. \qquad (7)$$

We also need two initial conditions $p_{sc}(r,\theta,0) = f(r,\theta)$ and $(p_{sc})_t(r,\theta,0) = g(r,\theta)$. The summarizing of our IBVP is given by

$$\text{PDE}: \quad (p_{sc})_{tt} = c^2\Big((p_{sc})_{rr} + \frac{(p_{sc})_r}{r} + \frac{(p_{sc})_{\theta\theta}}{r^2}\Big), \qquad (8)$$

$$\text{for } t > 0,\ r \in [a, r_\infty],\ \theta \in [0, 2\pi]$$

$$\text{BC } (r = a): \quad p_{sc}(a,\theta,t) = -e^{ika\cos(\theta-\rho)}e^{-iwt}, \qquad (9)$$

$$\text{for } t > 0,\ \theta \in [0, 2\pi]$$

$$\text{IC's } (t = 0): \quad p_{sc}(r,\theta,0) = f(r,\theta), \quad (p_{sc})_t(r,\theta,0) = g(r,\theta)$$

$$\text{Radiation Condition}: \quad (p_{sc})_t + c(p_{sc})_r \to 0, \quad \text{as } r \to \infty \qquad (10)$$

2.1 Analytical Solution for Circular Obstacle

The limiting amplitude principle establishes that as time grows, the solution of the scattering problem (8)-(10) with a periodic incident wave, e^{-iwt} will approximate a time harmonic wave with the same period. In fact,

$$\lim_{t\to\infty} p_{sc}(r,\theta,t) = \bar{p}_{sc}(r,\theta)e^{-iwt}, \qquad (11)$$

6

regardless of the initial conditions. It means the scattered wave separates in two functions when $t \to \infty$. One of them, $\bar{p}_{sc}$ is only a function of the space variables (r, θ) and the other is a harmonic function of time, e^{-iwt}.

Substitution of $p_{sc}(r, \theta, t)$ by $\bar{p}_{sc}(r, \theta)e^{-iwt}$ when $t \to \infty$ into PDE (8) leads to

$$-w^2 \bar{p}_{sc} e^{-iwt} = c^2 \nabla^2_{r,\theta} \bar{p}_{sc} e^{-iwt}.$$

Grouping the terms on one side, dividing by c^2 and factoring out the common exponential we get

$$\left[\nabla^2_{r,\theta} \bar{p}_{sc} + \frac{c^2}{w^2} \bar{p}_{sc} \right] e^{-iwt} = 0.$$

Recall that $w = c/k$ and since the exponential will never take on the value zero we can further reduce this to

$$\nabla^2_{r,\theta} \bar{p}_{sc} + k^2 \bar{p}_{sc} = 0.$$

Also the boundary condition (9) in the new independent variable $\bar{p}_{sc}$ reduces to

$$\bar{p}_{sc}(a, \theta) = -\bar{p}_{inc}(a, \theta) = -e^{ika \cos(\theta - \rho)},$$

while the radiation condition (10) reduces to

$$(\bar{p}_{sc})_r - ik\bar{p}_{sc} \to 0, \qquad \text{as } r \to \infty,$$

7

Therefore when $t \to \infty$ the IBVP (8)-(10) reduces to the BVP

$$\text{PDE}: \qquad \nabla_{r,\theta}^2 \bar{p}_{sc} + k^2 \bar{p}_{sc} = 0 \qquad\qquad (12)$$

$$\text{BC } (r = a): \qquad \bar{p}_{sc}(a, \theta) = -\bar{p}_{inc}(a, \theta) = -e^{ika \cos(\theta - \rho)} \qquad (13)$$

$$\text{Radiation Condition}: \qquad (\bar{p}_{sc})_r - ik\bar{p}_{sc} \to 0 \text{ as } r \to \infty \qquad (14)$$

The exact solution for this BVP can be computed by the method of separation of variables [10] and is given by

$$\bar{p}_{sc}(r, \theta) = \sum_{m=0}^{\infty} A_m H_m^{(1)}(kr) \cos(m\theta) \qquad (15)$$

where $H_m^{(1)}(kr)$ are cylindrical Hankel functions (see Appendix) of the first kind of order m. We assume the incident plane wave is propagating in the positive direction of the x-axis, therefore the angle of inclination of the incident wave $\rho = 0$. To determine the coefficients A_m, we start by finding the expansion of the spatial part of the incident wave in terms of kr and θ.

Proposition 1. *The Fourier expansion of the spatial part of the incident wave $\bar{p}_{inc}(r, \theta)$ in terms of the eigenfunctions $\{\cos(m\theta)\}$ and Bessel functions J_m of order m is given by*

$$\bar{p}_{inc}(r, \theta) = \sum_{m=0}^{\infty} \varepsilon_m i^m J_m(kr) \cos m\theta, \qquad (16)$$

where $\varepsilon_0 = 1$, $\varepsilon_m = 2$, for $m > 0$.

Proof: The fourier expansion of the spatial part of the incident wave in terms of the eigenfunctions $\{\cos(m\theta)\}$ and Bessel functions J_m of order m is given by

$$\bar{p}_{inc}(kr, \theta) = \sum_{m=0}^{\infty} C_m J_m(kr) \cos m\theta. \qquad (17)$$

The coefficients C_m are obtained from the orthogonality condition satisfied by the

8

eigenfunctions. In fact, assuming an angle of inclination $\rho = 0$, multiplying by the eigenfunctions and integrating gives

$$\int_0^{2\pi} p_{inc}(r,\theta) \cos m\theta d\theta = \int_0^{2\pi} e^{ikr\cos\theta} \cos m\theta d\theta \qquad (18)$$

$$= C_m J_m(kr) \int_0^{2\pi} \cos^2 m\theta d\theta = C_m J_m(kr) \cdot \begin{cases} 2\pi & \text{if } m = 0 \\ \pi & \text{if } m > 0. \end{cases}$$

The second integral can be computed from the following formula derived in [14]

$$\int_0^{2\pi} e^{iz\cos\theta} \cos m\theta d\theta = 2\pi i^m J_m(z).$$

Therefore,

$$\int_0^{2\pi} e^{ikr\cos\theta} \cos m\theta d\theta = 2\pi i^m J_m(kr),$$

Combining this equation with equation (18) results

$$C_m = \begin{cases} i^m, & \text{if } m = 0 \\ 2i^m, & \text{if } m > 0. \end{cases} \qquad (19)$$

Substitution of these C_m's values in (17) leads to the desired expansion

$$\bar{p}_{inc}(r,\theta) = \sum_{m=0}^{\infty} \varepsilon_m i^m J_m(kr) \cos m\theta, \qquad (20)$$

where $\varepsilon_0 = 1$, $\varepsilon_m = 2$, for $m > 0$. ∎

Then, substituting (15) and (16) with $r = a$ into the boundary condition (13), we get

$$\sum_{m=0}^{\infty} A_m H_m^{(1)}(ka) \cos(m\theta) = \bar{p}_{sc}(a,\theta) = -e^{ika\cos\theta} = -\sum_{m=0}^{\infty} \epsilon_m i^m J_m(ka) \cos(m\theta).$$

9

Since the expanded representations are unique, the coefficients must coincide. This gives

$$A_m = -\frac{\epsilon_m i^m J_m(ka)}{H_m^{(1)}(ka)}.$$

Substitution of these coefficients into (15) leads to the exact solution of the BVP (12)-(14) for $\bar{p}_{sc}(r,\theta)$, given by

$$\bar{p}_{sc}(r,\theta) = \sum_{m=0}^{\infty} \frac{-\epsilon_m i^m J_m(ka)}{H_m^{(1)}(ka)} H_m^{(1)}(kr) \cos(m\theta). \tag{21}$$

Summarizing, the solution of our time dependent IBVP (8)-(10) for an incident wave angle of inclination $\rho = 0$ satisfies (11) where $\bar{p}_{sc}(r,\theta)$ is defined by (21). The magnitude of the total amplitude pressure p when $t \to \infty$ can be calculated as

$$\big| p(r,\theta,t) \big| = \big| p_{sc}(r,\theta,t) + p_{inc}(r,\theta,t) \big| = \big| \bar{p}_{sc}(r,\theta)e^{-iwt} + e^{ikr\cos\theta}e^{-iwt} \big|$$
$$= \big| \bar{p}_{sc}(r,\theta) + e^{ikr\cos\theta} \big| \big| e^{-iwt} \big| = \big| \bar{p}_{sc}(r,\theta) + e^{ikr\cos\theta} \big|,$$

whose plot can be seen in Fig. (3).

An important physical measure of the energy scattered, the differential scattering cross section, can also be obtained. In fact, in 1956 Wilcox [12] showed that as $r \to \infty$

$$\bar{p}_{sc}(r,\theta) \to \frac{e^{ikr}}{r^{1/2}} \left[A_0(\theta) + \frac{A_1(\theta)}{r} \dots \right]. \tag{22}$$

The coefficient $A_0(\theta)$ of the leading order term of (22) is called the differential scattering cross section. It can be obtained from (22) neglecting higher order terms and is given by

$$A_0(\theta) = \sqrt{r}e^{-ikr}\bar{p}_{sc}(r,\theta). \tag{23}$$

10
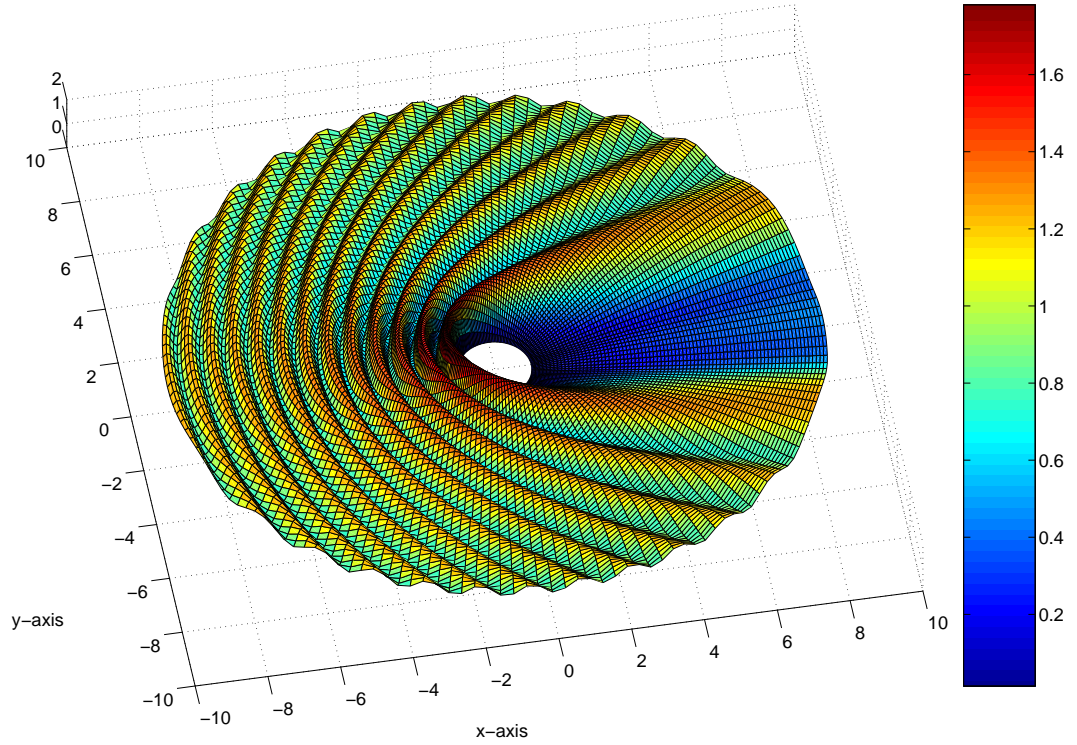
Figure 3: Analytical Solution of total pressure p on a 161×81 polar grid with $1 \leq r \leq 9$ and $\rho = 0$, when $t \to \infty$

The absolute value of $A_0(\theta)$ is usually called the far field amplitude of the scattered wave and can be calculated from (23) as

$$\left| A_0(\theta) \right| = \sqrt{r} \left| \bar{p}_{sc}(r, \theta) \right|, \qquad \text{as } r \to \infty.$$

2.2 Numerical Solution for Circular Obstacle in Polar Coordinates

To find a numerical solution of IBVP (8)-(10), we will adopt a finite differences time domain method [3] which consists of approximating all the derivatives in PDE (8) using their corresponding centered finite differences. Then, march in time until the

steady state solution is reached. This procedure has its theoretical basis in the limiting amplitude principle mentioned earlier, which establishes that the solution of (8)-(10) will reach a steady state harmonic in time.

In order to solve the IBVP (8)-(10) numerically, we need to replace the derivatives with their centered finite difference approximations. The computations will be performed on a polar grid. The angle θ will be partitioned using index i, so that $\theta_1 = 0$ and $\theta_{n_1} = 2\pi$. The radius r will be partitioned with index j so that $r_1 = a$ and $r_{n_2} = r_\infty$. Here r_∞ corresponds to a fictitious infinite boundary. This gives $\Delta\theta = 2\pi/(n_1 - 1)$ and $\Delta r = (r_\infty - a)/(n_2 - 1)$. To discretize the PDE (8) we use the following 3-point centered differences, whose orders are as follows

$$(p_{sc})_{tt} = \frac{1}{\Delta t^2}\Big((p_{sc})_{i,j}^{n+1} - 2(p_{sc})_{i,j}^n + (p_{sc})_{i,j}^{n-1}\Big) + \mathcal{O}(\Delta t^2) \qquad (24)$$

$$(p_{sc})_{rr} = \frac{1}{\Delta r^2}\Big((p_{sc})_{i,j+1}^n - 2(p_{sc})_{i,j}^n + (p_{sc})_{i,j-1}^n\Big) + \mathcal{O}(\Delta r^2)$$

$$(p_{sc})_r = \frac{1}{2\Delta r}\Big((p_{sc})_{i,j+1}^n - (p_{sc})_{i,j-1}^n\Big) + \mathcal{O}(\Delta r^2)$$

$$(p_{sc})_{\theta\theta} = \frac{1}{\Delta\theta^2}\Big((p_{sc})_{i+1,j}^n - 2(p_{sc})_{i,j}^n + (p_{sc})_{i-1,j}^n\Big) + \mathcal{O}(\Delta\theta^2)$$

For each step in time, the numerical computation is performed in three regions. The source of the energy is the incident plane wave p_{inc} and $p_{sc}(a,\theta) = -p_{inc}(a,\theta)$ along the boundary of the obstacle. Therefore, the computation starts at the obstacle boundary corresponding to $r = a$. This is the first region. Then, the computation moves to the second region where $a < r < r_\infty$. These are the interior points. The final computation is made in the third region where $r = r_\infty$ and where both the discretization of PDE (8) and the radiation condition (10) need to be combined. In order to improve the order of approximation at $r = r_\infty$, we will use an improved

12

radiation condition

$$(p_{sc})_t + c(p_{sc})_r + c\frac{p_{sc}}{2r} \to 0 \text{ as } r \to r_\infty, \tag{25}$$

whose derivation is given in the Appendix.

For a given level in time, the numerical computation begins at the boundary of the obstacle, $r = a$ which corresponds to index $j = 1$. For the boundary of the obstacle, p_{sc} is found by using the boundary condition (9) which is

$$p_{sc}(a, \theta) = -p_{inc}(a, \theta) = -e^{ika \cos(\theta - \rho)} e^{-iwt}. \tag{26}$$

The computations then move to the interior of the annulus, r_j and θ_i where $2 \leq j \leq n_2 - 1$ and $1 \leq i \leq n_1$. Plugging approximations (24) into equation (8) and solving for $(p_{sc})_{n+1}$, we obtain

$$
\begin{aligned}
(p_{sc})_{i,j}^{n+1} = {} & 2\Big(1 - d^2 - \frac{e^2}{r^2}\Big)(p_{sc})_{i,j}^n + d^2\Big(1 + \frac{\Delta r}{2r}\Big)(p_{sc})_{i,j+1}^n \\
& + d^2\Big(1 - \frac{\Delta r}{2r}\Big)(p_{sc})_{i,j-1}^n + \frac{e^2}{r^2}\Big((p_{sc})_{i+1,j}^n + (p_{sc})_{i-1,j}^n\Big) - (p_{sc})_{i,j}^{n-1}
\end{aligned}
\tag{27}
$$

where $d = c\Delta t/\Delta r$ and $e = c\Delta t/\Delta \theta$. Equation (27) is used to determine the value of the scattered wave for all interior points with continuity modifications at the branch cut. These modifications are as follows. Since the polar grid overlaps at the branch cut we have $x_{1,j} = x_{n_1,j}$ and $y_{1,j} = y_{n_1,j}$ for $j = 1, \ldots, n_2$. When $i = 1$ equation (27) runs into a problem because the value of $(p_{sc})_{i-1} = (p_{sc})_0$ is unknown. This point, while still in the physical domain, is not in the computational domain. This is overcome by using the value of its physical equivalent $(p_{sc})_{n_1-1}$ instead. There are no such problems for $i = 2, \ldots, n_1 - 1$. For $i = n_1$, we find the value of $(p_{sc})_{n+1}$ in equation (27) by setting it equal to its value at $i = 1$ to avoid recomputing p_{sc} at the same physical point. This correlation between indices $i = 0$ and $i = n_1 - 1$ is

13

illustrated in Fig. (17) in section 4.

The computation for the current level in time, $t = t_n$ is completed along the fictitious infinite boundary, $r = r_\infty$, which corresponds to index $j = n_2$. Along this boundary equation (27) fails because the value of $(p_{sc})_{n_2+1}$ is outside both the physical and computational domains. This is where the radiation condition comes in. First the improved radiation condition (25) is discretized using the approximations

$$(p_{sc})_t = \frac{1}{2\Delta t}\left((p_{sc})_{i,n_2}^{n+1} - (p_{sc})_{i,n_2}^{n-1}\right) + \mathcal{O}(\Delta t^2) \tag{28}$$

$$(p_{sc})_r = \frac{1}{2\Delta r}\left((p_{sc})_{i,n_2+1}^{n} - (p_{sc})_{i,n_2-1}^{n}\right) + \mathcal{O}(\Delta r^2) \tag{29}$$

Then it's solved for $(p_{sc})_{i,n_2+1}^{n}$. An equation for $(p_{sc})_{i,n_2}^{n+1}$ can be derived by inserting $(p_{sc})_{i,n_2+1}^{n}$ from the discretization of the radiation condition into equation (27) and resolving for $(p_{sc})_{i,n_2}^{n+1}$ to get

$$
\begin{aligned}
(p_{sc})_{i,n_2}^{n+1} = \left(1 + d + \frac{d\Delta r}{2r_\infty}\right)^{-1}&\left[\left(2 - 2d^2 - \frac{2e^2}{r^2} - \frac{d^2\Delta r}{r_\infty} - \frac{d^2\Delta r^2}{2r_\infty^2}\right)(p_{sc})_{i,n_2}^{n}\right. \\
&\left.+ 2d^2(p_{sc})_{i,n_2-1}^{n} + \frac{e^2}{r^2}\left((p_{sc})_{i+1,n_2}^{n} + (p_{sc})_{i-1,n_2}^{n}\right) + \left(d + \frac{d\Delta r}{2r_\infty} - 1\right)(p_{sc})_{i,n_2}^{n-1}\right],
\end{aligned}
\tag{30}
$$

for $i = 1, \ldots, n_1$ and where $d = c\Delta t/\Delta r$ and $e = c\Delta t/\Delta\theta$. Equation (30) is not dependent on $(p_{sc})_{i,n_2+1}^{n}$ and so is used to determine the value of the scattered wave for all outer edge points corresponding to $r = r_\infty$ with the same continuity modifications at the branch cut, as described for the interior points.

This completes the computations for one level in time over the entire computational domain, $(r, \theta) \in [a, r_\infty] \times [0, 2\pi]$. Levels in time are computed for $n = 1, 2, \ldots$ until the max point-wise difference between two successive levels in time fall below a specified tolerance ϵ. This uniform convergence is expressed as

$$\underset{i,j}{\text{Max}}\left|\,|(p_{sc})_{i,j}^{n}| - |(p_{sc})_{i,j}^{n-1}|\,\right| < \epsilon. \tag{31}$$

14

In summary, equations (27) and (30) are used together as we march in time to approximate the harmonic steady state of the scattered wave p_{sc}.

2.2.1 Stability Considerations. Courant, Friedrichs, and Levy Condition

As usual for hyperbolic equations, a way to establish a criteria for stability is based on Courant, Friedrichs, and Levy's theorem (CFL) [11]

Theorem 1. *A necessary condition for convergence of a finite difference scheme associated to a partial differential equation is that its domain of dependence contain the domain of dependence of the partial differential equation.*

This theorem can be supplemented by the Lax equivalence theorem, which basically states that for a properly posed IVP and a consistent finite difference approximation of it, stability is equivalent to convergence. In other words, CFL condition can also be considered as a condition for stability.

In cartesian coordinates, for the two-dimensional second order wave equation, the CFL condition [11] is

$$c\frac{\Delta t}{\Delta x} \leq 1, \quad \text{and} \quad c\frac{\Delta t}{\Delta y} \leq 1. \tag{32}$$

This condition in terms of polar coordinates is written as

$$c\frac{\Delta t}{\Delta r} \leq 1, \quad \text{and} \quad c\frac{\Delta t}{r\Delta\theta} \leq 1. \tag{33}$$

Another interpretation of the CFL condition for hyperbolic equations is that the numerical wave speed should be larger than the physical wave speed. This condition will guarantee that the domain of dependence of the numerical scheme contains the domain of dependence of the PDE. In our numerical simulation contained in the next section, Δt, Δr and $\Delta\theta$ were selected according to the CFL condition.

15

2.2.2 Results
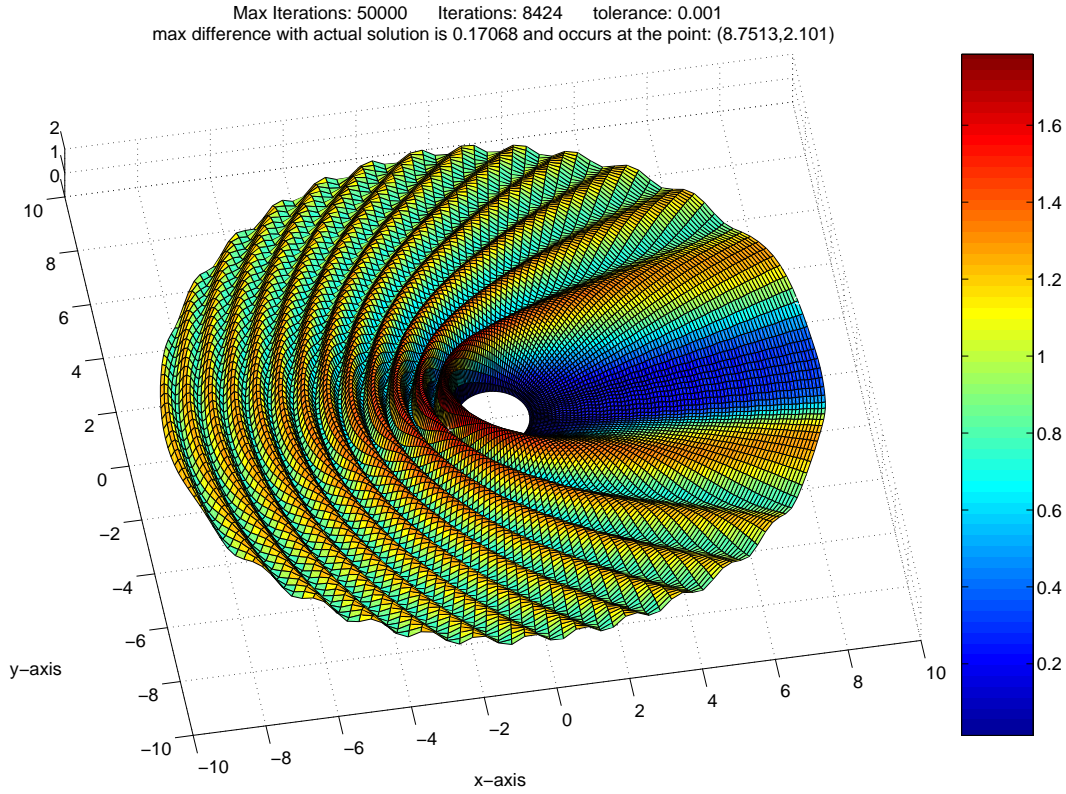
Figure 4: Numerical Solution using polar coordinates with $\Delta r = 0.1$, $\Delta \theta = \pi/80$, and $\Delta t = 0.01$

Using polar coordinates, the solution to IBVP (8)-(10) is approximated and gives results whose accuracy and stability depend on the spacing in the polar grid. The magnitude of the total pressure is computed using the numerical solution for the scattered wave p_{sc} and can be viewed in Fig. (4). It is obvious from the plot that the numerical solution is a near mirror image of the analytical solution seen in Fig. (3). The numerical solution is compared to the analytical solution by comparing their plots along a fixed angle or radius. Fig. (5) shows the comparison along the angle, $\theta = \pi/3$ and the comparison of the scattering cross sections. The numerical solution can also be compared point-wise with the analytical solution. To determine

16
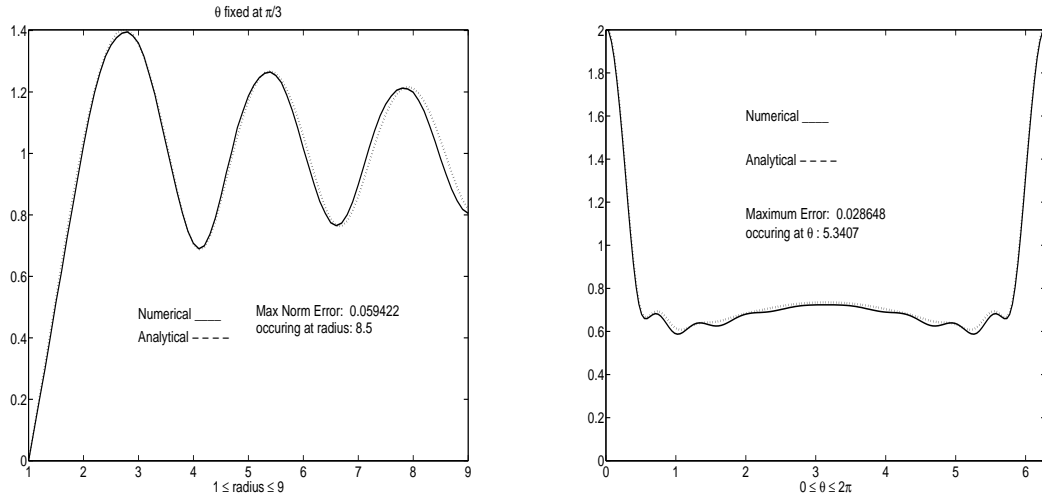
Figure 5: Comparison of Numerical Solution computed using polar coordinates to Analytical Solution for $\theta = \pi/3$ and Comparison of scattering cross sections

the average error between the two solutions we compute average of the point-wise differences between the numerical and analytical solutions. The average point-wise error between the numerical and analytical solutions is 0.0318, which is minimal. The focus of this paper is to get solutions for the scattering of acoustic waves from cylinders of arbitrary cross-section using curvilinear coordinates whose coordinate lines fit the boundary of the obstacle. Therefore, in the next section, we discuss algorithms to numerically generate boundary conforming grids.

3   Winslow's Method for the Automatic Generation of Boundary Conforming Curvilinear Coordinates

In order to create different coordinate systems which conform to arbitrary shapes, we use elliptic grid generators. Amsden and Hirt [13] developed a method using the

17

solutions of the system of elliptic PDE's

$$\nabla^2 x = x_{\xi\xi} + x_{\eta\eta} = 0 \qquad\qquad \nabla^2 y = y_{\xi\xi} + y_{\eta\eta} = 0 \qquad (34)$$

to generate grids depicting a transformation from a computational rectangular domain $\mathcal{D}'$ to a physical domain $\mathcal{D}$. The problem with Amsden-Hirt's method is that if the physical domain $\mathcal{D}$ is not convex then the grid generated tends to overlap, thus giving a transformation which is not one-to-one. This can be seen in Fig. (6). In 1966,
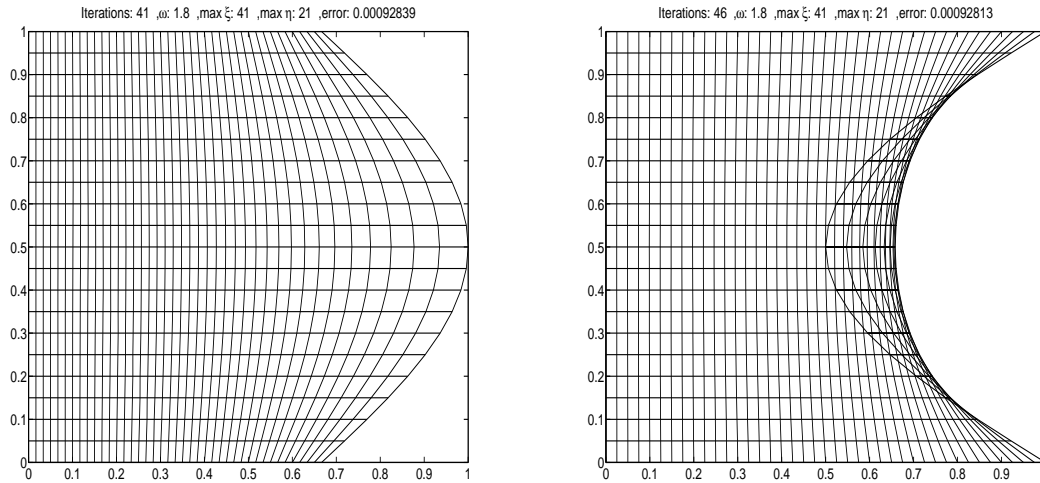
Figure 6: Grids made using Amsden-Hirt generator.

Winslow [5] introduced a novel technique to obtain boundary conforming coordinates. To get a non-overlapping, one-to-one transformation. We consider a Amsden-Hirt transformation from the physical domain $\mathcal{D}$ to the computational domain $\mathcal{D}'$.

$$\mathcal{T} : \mathcal{D} \to \mathcal{D}'$$
$$\mathcal{T} : (x, y) \mapsto (\xi, \eta),$$

18

defined by

$$\nabla^2\xi = \xi_{xx} + \xi_{yy} = 0 \qquad\qquad \nabla^2\eta = \eta_{xx} + \eta_{yy} = 0, \qquad (35)$$

It is difficult to numerically solve Winslow equations on an arbitrary physical domain directly. However, a convenient numerical algorithm can be obtained if the Winslow transformation is inverted (assuming the Jacobian of the transformation is not zero). The result of inverting (35) is

$$\alpha x_{\xi\xi} - 2\beta x_{\xi\eta} + \gamma x_{\eta\eta} = 0 \qquad (36)$$

$$\alpha y_{\xi\xi} - 2\beta y_{\xi\eta} + \gamma y_{\eta\eta} = 0.$$

where $\alpha = x_\eta^2 + y_\eta^2$, $\beta = x_\xi x_\eta + y_\xi y_\eta$, and $\gamma = x_\xi^2 + y_\xi^2$ are scale metric factors of the transformation T. Winslow's method uses the solutions to the system (36) to generate grids which, in general, do not overlap. A detailed account of Winslow and elliptic grid generators can be found in [2]. Fig. (7) shows the results of Winslow's grid generating method which can be compared to Amsden-Hirt's in Fig. (6). In this work, we will use
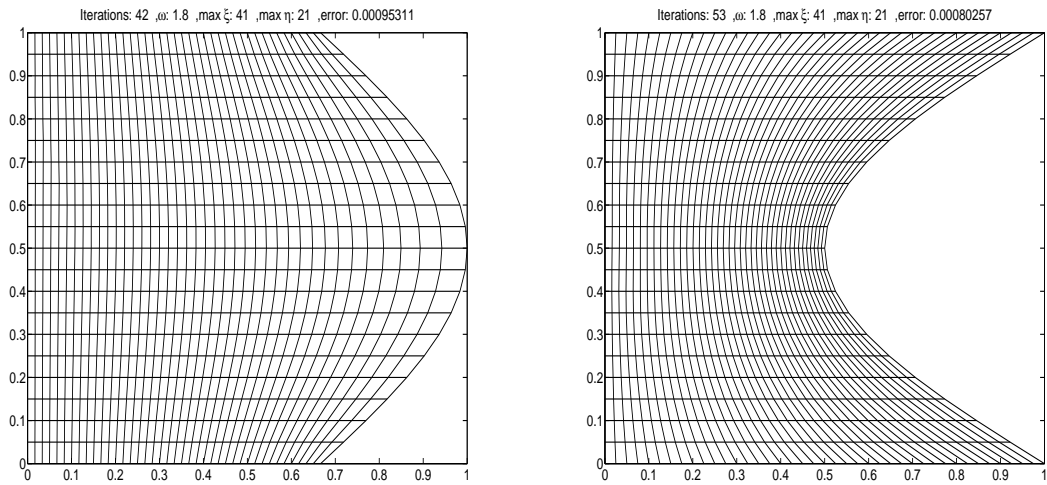
Figure 7: Grids made using Winslow generator.

19

Winslow's algorithm to generate two-dimensional boundary conforming coordinates, over multiply-connected regions. We now consider an invertible transformation $T : \mathcal{D}' \to \mathcal{D}$, from a rectangular computational domain $\mathcal{D}'$ with coordinates (ξ, η) to the physical multiply connected domain $\mathcal{D}$ of arbitrary shape with coordinates (x, y). The transformation T, seen in Fig. (8), is defined as $T(\xi, \eta) = \big(x(\xi, \eta), y(\xi, \eta)\big)$, where the computational domain $\mathcal{D}'$ is formed by all pairs (ξ, η) such that $\Delta \xi = 1$ and $\Delta \eta = 1$. The choice of spacing in the computational domain $\mathcal{D}'$ is deliberate so as to simplify
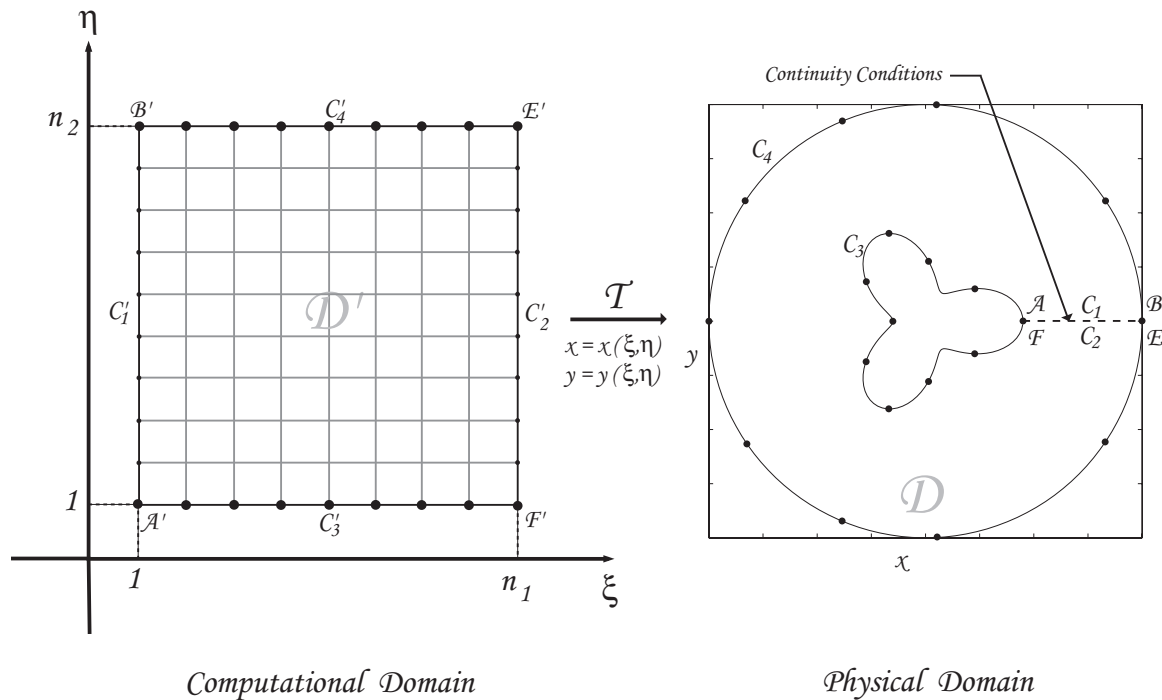
Figure 8: Transformation from Computational Domain $\mathcal{D}'$ to a Multiply-Connected Physical Domain $\mathcal{D}$ of Arbitrary Shape

the computations giving $\xi_i = \xi_o + (i-1)\Delta \xi = 1 + (i-1) = i$. Similarly the jth value of η is simply given by the index j.

The boundary value problems are finalized by defining boundary conditions over

the arbitrary boundary, C_3 (corresponding to $\eta = 1$), and over the outer circular boundary C_4 (corresponding to $\eta = n_2$). In Fig. (8), these Dirichlet boundary conditions are illustrated by dot points. The segment, $C_1 = C_2$, in Fig. (8) (corresponding to the lines $\xi = 1$ and $\xi = n_1$), represents the branch cut which is used to transform the multiply-connected physical domain $\mathcal{D}$ into a topologically equivalent connected rectangular computational domain $\mathcal{D}'$. Grid generation algorithms based on Winslow equations treat the branch cut as an interface over which the coordinates $\big(x(\xi,\eta), y(\xi,\eta)\big)$ and all their derivatives are continuous (continuity conditions). The elliptic system (36) on the computational domain with the above boundary and branch cut conditions is solved numerically. As a consequence, a boundary conforming curvilinear grid is obtained in the physical domain as an image of a previously defined uniform rectangular grid in the computational domain. Fig. (9) shows a curvilinear grid conforming to a 3-petal rose which was obtained applying Winslow algorithm to a rectangular grid composed of 11 horizontal lines and 41 vertical lines in the computational domain.
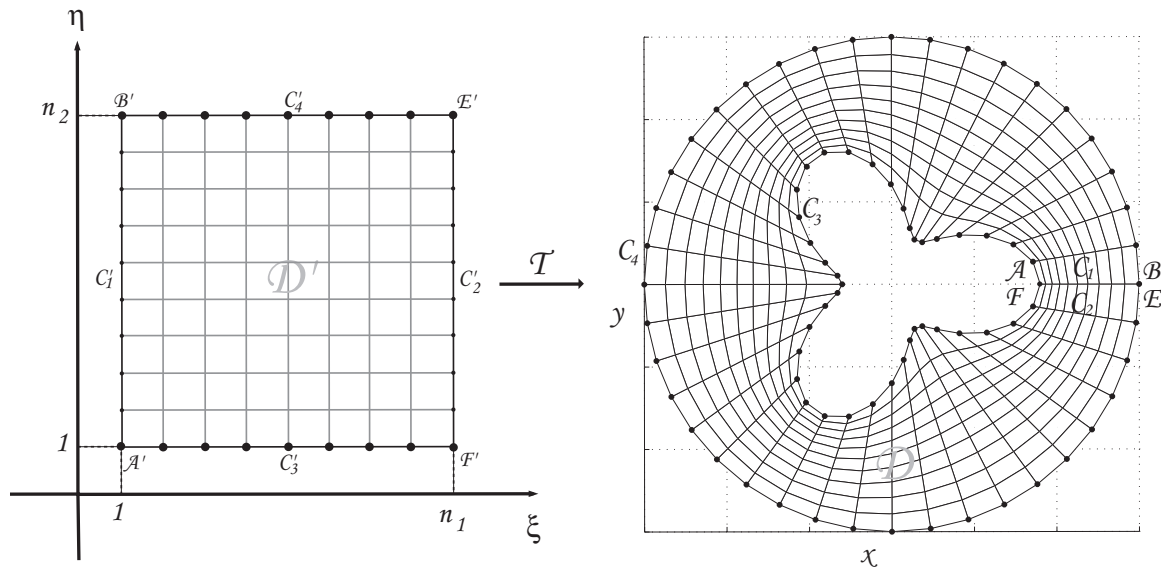
Figure 9: Boundary-Conforming grid curves obtained by applying Winslow algorithm.

To solve the system of elliptic PDE's (36) with the boundary and branch cut conditions mentioned before, we use finite difference schemes. The values of α, β and γ are approximated for each point using the centered finite differences

$$x_\xi = \frac{1}{2}\left(x_{i+1,j} - x_{i-1,j}\right) + \mathcal{O}(\Delta\xi^2)$$

$$y_\xi = \frac{1}{2}\left(y_{i+1,j} - y_{i-1,j}\right) + \mathcal{O}(\Delta\xi^2)$$

$$x_\eta = \frac{1}{2}\left(x_{i,j+1} - x_{i,j-1}\right) + \mathcal{O}(\Delta\eta^2)$$

$$y_\eta = \frac{1}{2}\left(y_{i,j+1} - y_{i,j-1}\right) + \mathcal{O}(\Delta\eta^2).$$

In order to numerically solve the system of equations (36) we also use

$$x_{\xi\xi} = x_{i-1,j} - 2x_{i,j} + x_{i+1,j} + \mathcal{O}(\Delta\xi^2)$$

$$y_{\xi\xi} = y_{i-1,j} - 2y_{i,j} + y_{i+1,j} + \mathcal{O}(\Delta\xi^2)$$

$$x_{\eta\eta} = x_{i,j-1} - 2x_{i,j} + x_{i,j+1} + \mathcal{O}(\Delta\eta^2)$$

$$y_{\eta\eta} = y_{i,j-1} - 2y_{i,j} + y_{i,j+1} + \mathcal{O}(\Delta\eta^2)$$

$$x_{\xi\eta} = \frac{1}{4}\left(x_{i+1,j+1} - x_{i+1,j-1} - x_{i-1,j+1} + x_{i-1,j-1}\right) + \mathcal{O}(\Delta\xi\Delta\eta)$$

$$y_{\xi\eta} = \frac{1}{4}\left(y_{i+1,j+1} - y_{i+1,j-1} - y_{i-1,j+1} + y_{i-1,j-1}\right) + \mathcal{O}(\Delta\xi\Delta\eta).$$

An initial grid is determined and then the grid is recomputed again and again until the max point-wise difference in successive grids drops below a specified tolerance. The points of the grid along the boundary of the obstacle (corresponding to $j = 1$) and along the outermost ring $(j = n_2)$ are fixed. Each point of a grid (x, y) is indexed by i and j which indicate which ray and ring, respectively, the computation is being performed on. Also an index k is needed to indicate the computation of the kth grid following the initial grid. Entire grids are generated one at a time by computing along the rays, from ray 1 to ray n_1. We will use Gauss-Sidel combined with SOR iteration

22

to compute point after point, one grid at a time. Using Gauss-Seidel iteration we get

$$\hat{x}_{i,j}^{(k)} = \frac{1}{2(\alpha + \gamma)} \Bigg[\alpha(x_{i-1,j}^{(k)} + x_{i+1,j}^{(k-1)}) \tag{37}$$
$$- \frac{\beta}{2} \Big(x_{i+1,j+1}^{(k-1)} - x_{i+1,j-1}^{(k-1)} - x_{i-1,j+1}^{(k)} + x_{i-1,j-1}^{(k)} \Big)$$
$$+ \gamma(x_{i,j-1}^{(k)} + x_{i,j+1}^{(k-1)}) \Bigg]$$

$$\hat{y}_{i,j}^{(k)} = \frac{1}{2(\alpha + \gamma)} \Bigg[\alpha(y_{i-1,j}^{(k)} + y_{i+1,j}^{(k-1)}) \tag{38}$$
$$- \frac{\beta}{2} \Big(y_{i+1,j+1}^{(k-1)} - y_{i+1,j-1}^{(k-1)} - y_{i-1,j+1}^{(k)} + y_{i-1,j-1}^{(k)} \Big)$$
$$+ \gamma(y_{i,j-1}^{(k)} + y_{i,j+1}^{(k-1)}) \Bigg]$$

where $\hat{x}_{i,j}^{(k)}$ and $\hat{y}_{i,j}^{(k)}$ are computed for $j = 2, \ldots, n_2 - 1$ and for $i = 2, \ldots, n_1 - 1$. $x_{i,j}^{(k)}$ indicates that the value of x at that location indexed by i and j is being taken from the current or k^{th} grid while $x_{i,j}^{(k-1)}$ indicates that the value of x at that location is being taken from the previous grid. This is Gauss-Seidel iteration. At the branch cut ($i = 1$ and $i = n_1$) continuity conditions are needed because the equations (37) and (38) depend on points which are in the physical domain $\mathcal{D}$ but not in the computational domain $\mathcal{D}'$. In the physical domain the values of (x, y) need to coincide for $i = 1$ and $i = n_1$ since these points lie along the branch cut as seen in figure (17) in the next section. When $i = 1$ the values of $x_{i-1,j}$ and $y_{i-1,j}$ in equations (37) and (38) are determined by instead using their physical equivalents $x_{n_1-1,j}$ and $y_{n_1-1,j}$. When $i = n_1$ the points (x, y) are set equal to those for $i = 1$. To enhance the convergence of the grids, equations (37) and (38) are computed hand in hand with SOR iteration and a relaxation parameter of $\omega \approx 1.85$ to get

$$x_{i,j}^{(k)} = \omega \hat{x}_{i,j}^{(k)} + (1 - \omega) x_{i,j}^{(k-1)} \tag{39}$$

$$y_{i,j}^{(k)} = \omega \hat{y}_{i,j}^{(k)} + (1 - \omega) y_{i,j}^{(k-1)}, \tag{40}$$

for $i = 2, \ldots, n_1$ and $j = 2, \ldots, n_2 - 1$. Given a specified tolerance ϵ, $x_{i,j}^{(k)}$ and $y_{i,j}^{(k)}$ from equations (39) and (40) are computed independently and used to generate successive grids $(k = 1, 2, 3, \ldots)$ over the entire computational domain $\mathcal{D}'$ until

$$\underset{i,j}{\text{Max}}\sqrt{\left(x_{i,j}^{(k)} - x_{i,j}^{(k-1)}\right)^2 + \left(y_{i,j}^{(k)} - y_{i,j}^{(k-1)}\right)^2} < \epsilon. \tag{41}$$

Once the tolerance criterion is met then $\left(x_{i,j}^{(k)}, y_{i,j}^{(k)}\right)$ can be plotted for $i = 1, \ldots, n_1$ and $j = 1, \ldots, n_2$.

3.1 Winslow Grid Generation Results
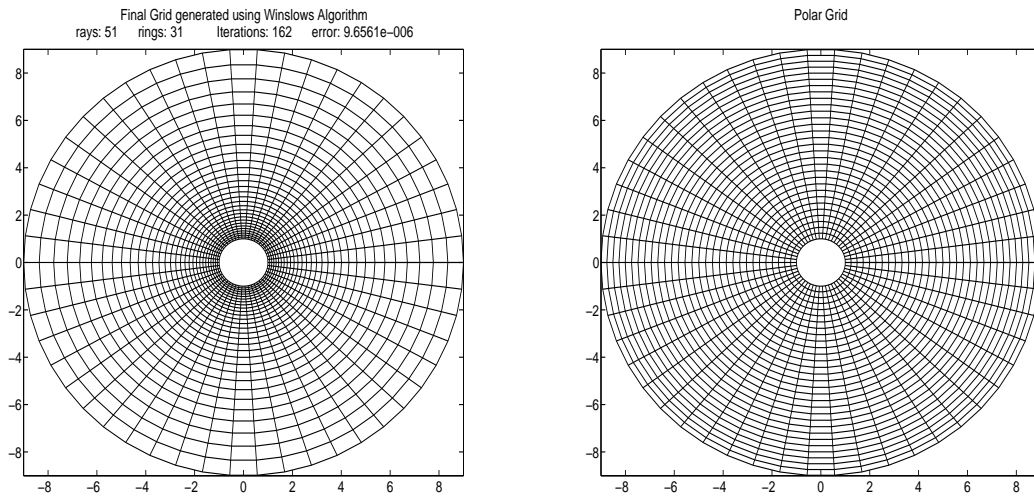
Figure 10: Winslow Grid of circular cross-section compared to a Polar Grid

The winslow grid for the circular cylinder can be used as a substitute for a polar grid when solving the IBVP modeling the dispersion of the plane wave. The accuracy of the numerical solution using Winslow's grid will be determined by comparing it to the analytical solution using a polar grid. These two grids seen in Fig. (10) differ in that the partition of the radius in the Winslow grid is not regular like that of the polar grid.

24
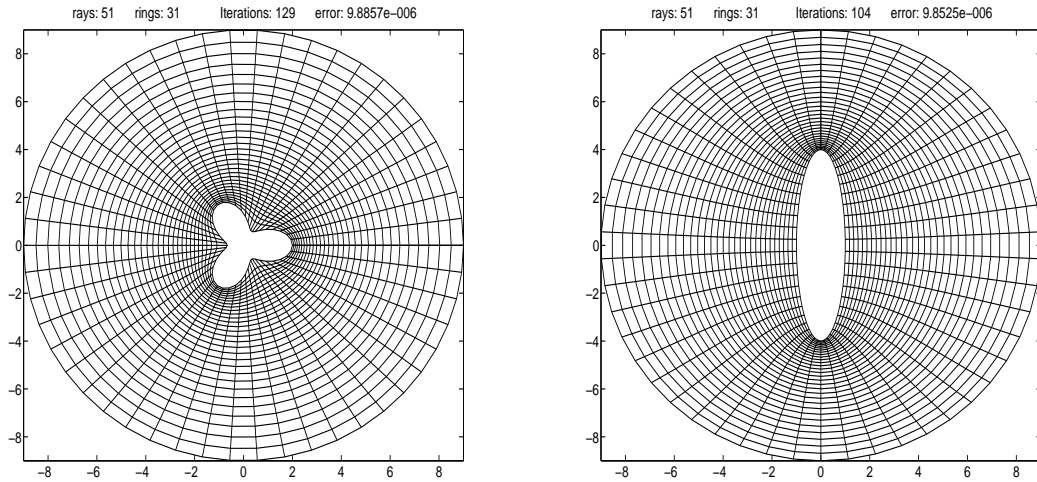
Figure 11: Winslow Grids of rose and elliptical cross-sections

The Winslow method can be used to generate smooth grids for a variety of boundary conditions. These grids have no folding and are one-to-one and thus provide good foundations for the numerical solutions to the IBVP modeling the dispersion of the plane wave. A sample of such smooth grids which don't overlap can be seen in Fig. (11).
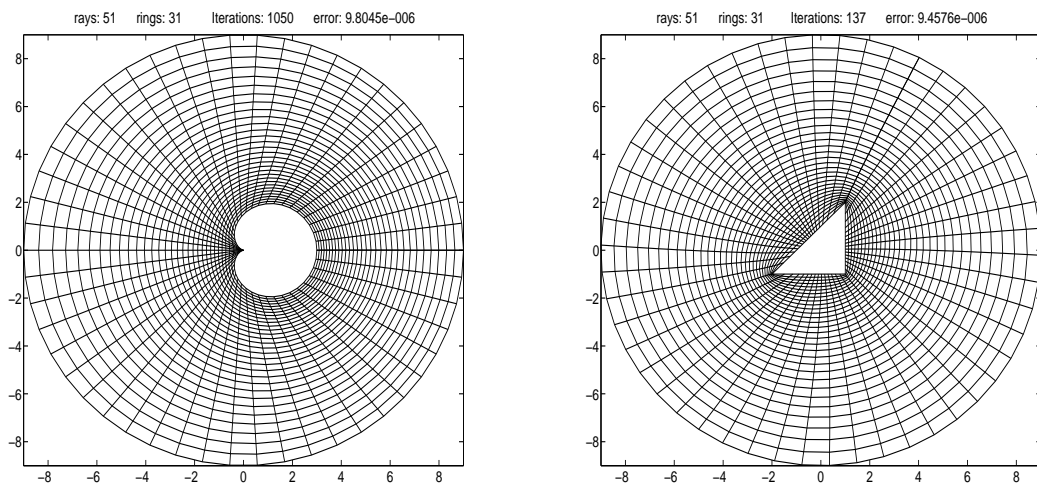
Figure 12: Winslow Grids of limacon and triangular cross-sections

25

Winslow's method generates smooth grids even near points along the boundary which are not differentiable such as the vertex of the limacon and the three vertices of the triangle as seen in Fig. (12).
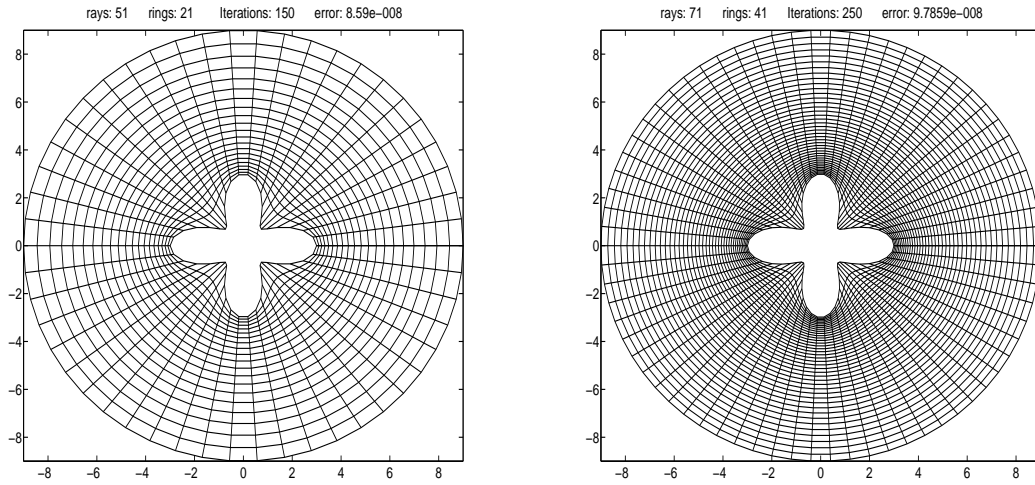
Figure 13: Winslow Grids of 4-petal cross section of varying grid meshing
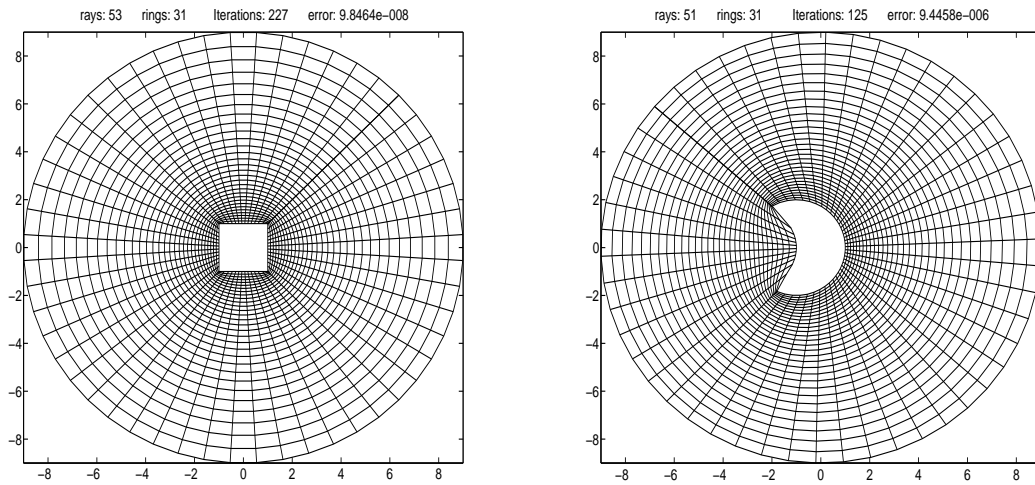
Figure 14: Winslow grids of square and crescent cross sections

It can be seen that Winslow's method doesn't seem to generate a refined grid in the pits of the 4-pedal rose. A larger number of rays and rings partially corrects this

26
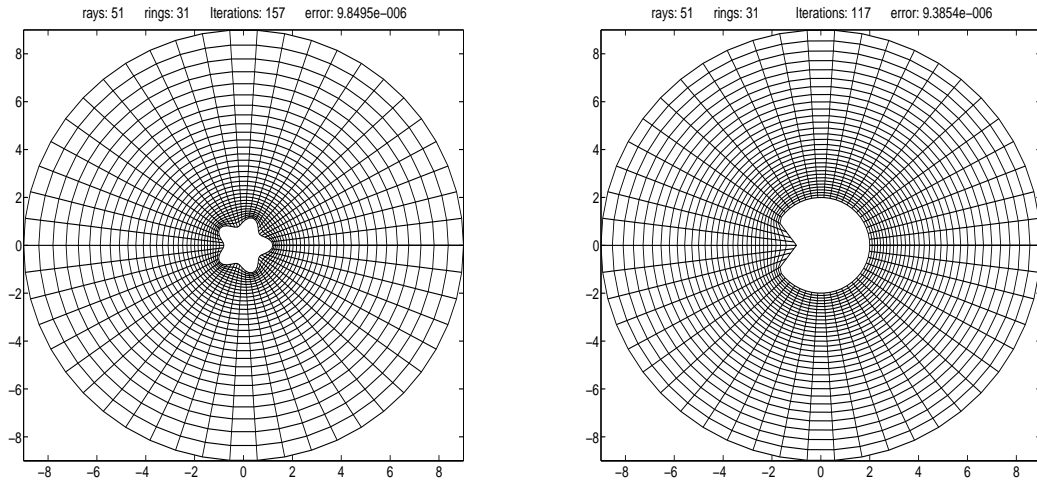
Figure 15: Winslow Grids of flower and pacman cross sections

problem as shown in Fig. (13). Other grids can be viewed in Fig. (14) and Fig. (15).

4 Wave Scattering from Infinite Cylindrical Obstacles of Arbitrary Cross-Section

In section 2.2, we studied a wave scattering initial boundary value problem, IBVP (8)-(10), for obstacles of circular cross-section. The natural coordinate system used in that case was a polar coordinate system. Both the analytical solution and finite differences time domain (FDTD) approximations were obtained and compared. In this section, we want to extend the study to cylindrical obstacle with arbitrary cross-section. In this case, analytical solutions are no longer available. Therefore, there is a need to obtain numerical approximations of the solution. Our approach is based on finite differences approximations of the wave equation and the boundary conditions. Since we want to solve problems where the boundary of the obstacle is of arbitrary shape, we will use boundary conforming coordinates (ξ, η) as independent variables. Then, we will implement our FDTD method over this new curvilinear coordinates.

27

This method, also called time dependent boundary-conforming coordinates method or simply TD-BCC, was used in paper [6] to numerically model scattering from prototypical antennas. In section 3, we described how to generate boundary conforming coordinates using elliptic grid generators. Actually, we obtained boundary conforming coordinates over different multiply connected domains with a single hole of arbitrary shape and a circular outer boundary. In this section, we compute the scattered and total field over those grids. Recall that the choice of spacing in the computational domain $\mathcal{D}'$ is $\Delta\xi = 1$ and $\Delta\eta = 1$. This choice is deliberate so as to simplify the computations giving $\xi_i = \xi_o + (i-1)\Delta\xi = 1 + (i-1) = i$. Similarly the jth value of η is simply given by the index j. Thus we can use the indices i and j as the values of ξ and η in the computational domain $\mathcal{D}'$ and as references to the x and y coordinates of the physical domain $\mathcal{D}$ as shown in Fig. (16).
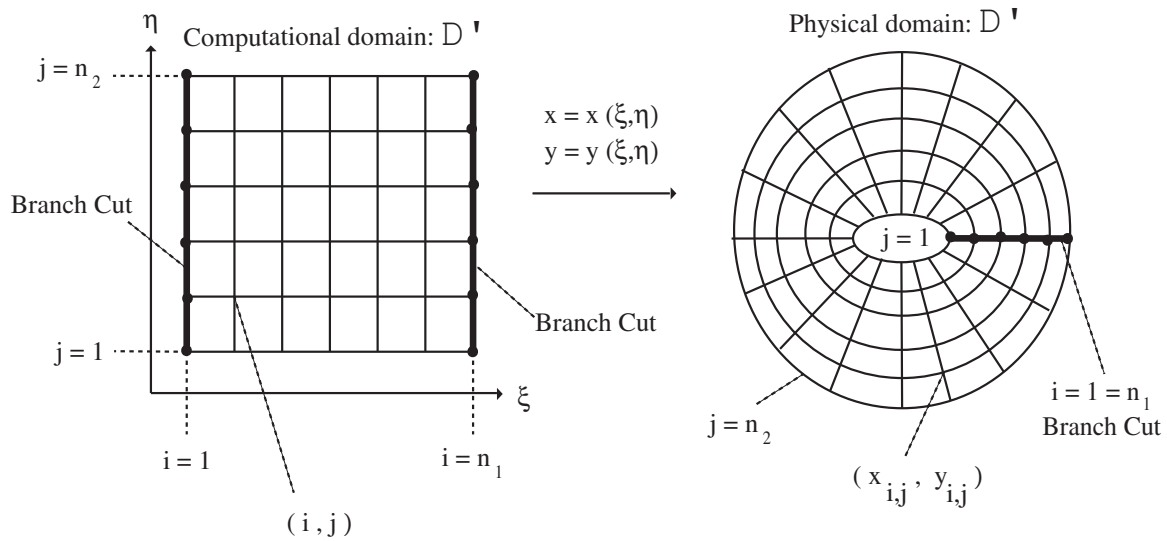
Figure 16: Transformation from a grid where $(\xi, \eta) = (i, j) \in [1, n_1] \times [1, n_2]$ to a physical domain with coordinates $(x_{i,j}, y_{i,j})$

To start, we need to express our IBVP in terms of the boundary conforming

28

coordinates. For example, the wave equation can be written as

$$p_{tt} = c^2 \nabla^2 p = c^2 \Big(p_{xx} + p_{yy} \Big) \tag{42}$$

$$= \frac{c^2}{J^2} \Big(\alpha p_{\xi\xi} - 2\beta p_{\xi\eta} + \gamma p_{\eta\eta} \Big)$$

$$+ \frac{c^2}{J^3} \bigg[\Big(\alpha y_{\xi\xi} - 2\beta y_{\xi\eta} + \gamma y_{\eta\eta} \Big)(x_\eta p_\xi - x_\xi p_\eta)$$

$$+ \Big(\alpha x_{\xi\xi} - 2\beta x_{\xi\eta} + \gamma x_{\eta\eta} \Big)(y_\xi p_\eta - y_\eta p_\xi) \bigg]$$

for $t > 0$, $1 \le \xi \le n_1$, and $1 \le \eta \le n_2$ and where $\alpha = x_\eta^2 + y_\eta^2$, $\beta = x_\xi x_\eta + y_\xi y_\eta$, and $\gamma = x_\xi^2 + y_\xi^2$ are the metric scale factors and $J = x_\xi y_\eta - x_\eta y_\xi$ is the Jacobian of the transformation $\mathcal{T}$. The derivation of this formula is in the Appendix. This is a rather bulky PDE to solve. However, if the grid generator is Winslow then the x and y-coordinates of the grid satisfy the elliptic system of PDE's used to generate them. Namely they satisfy

$$\Big(\alpha x_{\xi\xi} - 2\beta x_{\xi\eta} + \gamma x_{\eta\eta} \Big) = 0 \qquad \Big(\alpha y_{\xi\xi} - 2\beta y_{\xi\eta} + \gamma y_{\eta\eta} \Big) = 0. \tag{43}$$

Therefore the wave equation (42) simplifies to

$$p_{tt} = \frac{c^2}{J^2} \Big(\alpha p_{\xi\xi} - 2\beta p_{\xi\eta} + \gamma p_{\eta\eta} \Big), \tag{44}$$

for $t > 0$, $1 \le \xi \le n_1$, and $1 \le \eta \le n_2$. We now need to find a reformulation of the IBVP (8)-(10) in terms of the new curvilinear coordinates generated using Winslow's algorithm. In generalized curvilinear coordinates and with angle of inclination ρ the incident wave is given by

$$p_{inc}\big(x(\xi,\eta), y(\xi,\eta), t\big) = e^{ik\big(x(\xi,\eta)\cos\rho + y(\xi,\eta)\sin\rho\big)} e^{-iwt}. \tag{45}$$

29

The condition along the boundary of the obstacle is still given by $p_{sc} = -p_{inc}$. The improved Sommerfeld radiation condition (25) becomes

$$(p_{sc})_t + \frac{c}{Jr}\Big(\lambda(p_{sc})_\xi + \kappa(p_{sc})_\eta\Big) + \frac{cp_{sc}}{2r} \to 0 \text{ as } r \to \infty \qquad (46)$$

where $\lambda = xy_\eta - yx_\eta$ and $\kappa = yx_\xi - xy_\xi$ and $r = r_\infty$ is a fictitious infinite boundary. As a result the IBVP for the scattered wave problem is

$$\text{PDE}: \qquad (p_{sc})_{tt} = \frac{c^2}{J^2}\Big(\alpha(p_{sc})_{\xi\xi} - 2\beta(p_{sc})_{\xi\eta} + \gamma(p_{sc})_{\eta\eta}\Big), \qquad (47)$$

$$\text{for } t > 0, \ 1 \le \xi \le n_1, \ 1 \le \eta \le n_2$$

$$\text{BC } (\eta = j = 1): \qquad p_{sc} = -p_{inc} = -e^{ik\big(x(\xi,1)\cos\rho + y(\xi,1)\sin\rho\big)}e^{-iwt}, \qquad (48)$$

$$\text{for } t > 0, \ 1 \le \xi \le n_1$$

$$\text{IC's } (t = 0): \qquad p_{sc} = 0, \qquad (p_{sc})_t = 0$$

$$\text{Radiation Condition}: \qquad (p_{sc})_t + \frac{c}{Jr}\Big(\lambda(p_{sc})_\xi + \kappa(p_{sc})_\eta\Big) + \frac{cp_{sc}}{2r} \to 0 \qquad (49)$$

$$\text{as } r \to \infty$$

This paper now explores the use of finite difference methods to solve the IBVP (47)-(49) expressed in curvilinear coordinates. Firstly, a lower order 3-point derivative approximating scheme is used and secondly a higher order 5-point scheme is attempted.

4.1   Lower Order 3-Point Scheme

In order to numerically solve the PDE (44) we need to discretize the equation using finite difference methods. The numerical computation proceeds as it did for the polar numerical computation in section 2.2. The initial conditions give $p_{sc} = 0$, except at the boundary, for the first time level, $n = 1$. So we start our computations at the second level. Because we are using a centered 3-point scheme for the derivative with

30

respect to time t, to compute any level in time requires data from the previous two levels in time. To compute the second level in time we need to impose a ghost level which precedes the first level and which has the condition $p_{sc} = 0$.

For a given time level our computation begins on the boundary corresponding to $j = 1$ and $1 \leq i \leq n_1$. For the boundary of the obstacle we find p_{sc} at any time by using the boundary condition (48).

We now move the computation to the interior, $1 \leq i \leq n_1$ and $2 \leq j \leq n_2 - 1$. To approximate the scale metric factors α, β and γ we use the following centered finite differences:

$$
\begin{aligned}
x_\xi &= \frac{1}{2}\Big(x_{i+1,j} - x_{i-1,j}\Big) + \mathcal{O}(\Delta\xi^2) \\
x_\eta &= \frac{1}{2}\Big(x_{i,j+1} - x_{i,j-1}\Big) + \mathcal{O}(\Delta\eta^2) \\
y_\xi &= \frac{1}{2}\Big(y_{i+1,j} - y_{i-1,j}\Big) + \mathcal{O}(\Delta\xi^2) \\
y_\eta &= \frac{1}{2}\Big(y_{i,j+1} - y_{i,j-1}\Big) + \mathcal{O}(\Delta\eta^2)
\end{aligned}
$$

In order to numerically solve the PDE (44) we also need the following:

$$
(p_{sc})_{tt} = \frac{1}{\Delta t^2}\Big((p_{sc})_{i,j}^{n+1} - 2(p_{sc})_{i,j}^n + (p_{sc})_{i,j}^{n-1}\Big) + \mathcal{O}(\Delta t^2)
$$

$$
(p_{sc})_{\xi\xi} = (p_{sc})_{i+1,j}{}^n - 2(p_{sc})_{i,j}^n + (p_{sc})_{i-1,j}^n + \mathcal{O}(\Delta\xi^2)
$$

$$
(p_{sc})_{\eta\eta} = (p_{sc})_{i,j+1}^n - 2(p_{sc})_{i,j}^n + (p_{sc})_{i,j-1}^n + \mathcal{O}(\Delta\eta^2)
$$

$$
(p_{sc})_{\xi\eta} = \frac{1}{4}\Big((p_{sc})_{i+1,j+1}^n - (p_{sc})_{i+1,j-1}^n - (p_{sc})_{i-1,j+1}^n + (p_{sc})_{i-1,j-1}^n\Big) + \mathcal{O}(\Delta\xi\Delta\eta)
$$

Since we are computing along the interior rings these centered 3-point approximations never leave the physical domain. Plugging these approximations into equation (44)

31

and solving for $(p_{sc})_{n+1}$, we obtain

$$(p_{sc})_{i,j}^{n+1} = 2\left(1 - \alpha\delta^2 - \gamma\delta^2\right)(p_{sc})_{i,j}^n + \delta^2\left[\alpha\left((p_{sc})_{i-1,j}^n + (p_{sc})_{i+1,j}^n\right)\right. \tag{50}$$

$$-\frac{\beta}{2}\left((p_{sc})_{i+1,j+1}^n - (p_{sc})_{i+1,j-1}^n - (p_{sc})_{i-1,j+1}^n + (p_{sc})_{i-1,j-1}^n\right)$$

$$\left. + \gamma\left((p_{sc})_{i,j-1}^n + (p_{sc})_{i,j+1}^n\right)\right] - (p_{sc})_{i,j}^{n-1}$$

for $1 \leq i \leq n_1$ and $2 \leq j \leq n_2 - 1$ and where $\delta = c\Delta t/J$. Equation (50) is used to determine the value of the scattered wave for all interior points. At the branch cut ($i = 1$ and $i = n_1$) continuity conditions are needed because equation (50) depends on points which are in the physical domain $\mathcal{D}$ but not in the computational domain $\mathcal{D}'$. In the physical domain the value of p_{sc} and its derivatives in the direction of ξ need to coincide along the segments when $i = 1$ and $i = n_1$ since these points lie along the branch cut and hence represent the same physical points. When $i = 1$ the value of $(p_{sc})_{i-1,j}^n = (p_{sc})_{0,j}^n$ in equation (50) is determined by instead using its physical equivalent $(p_{sc})_{n_1-1,j}^n$. This correlation between the indices $i = 0$ and $i = n_1 - 1$ is illustrated in Fig. (17). When $i = n_1$ the value of p_{sc} is set equal to its value for $i = 1$ to avoid computation of the same physical points. Similar modifications are made for the approximations of the derivatives in the direction of ξ for the coordinates x and y.

The computation now moves to the fictitious infinite boundary, $r = r_\infty$, corresponding to the indices $j = n_2$ and $1 \leq i \leq n_1$. At $r = r_\infty$, equation (50) depends on the values of $(p_{sc})_{i,n_2+1}^n$, $(p_{sc})_{i-1,n_2+1}^n$, and $(p_{sc})_{i+1,n_2+1}^n$, which are all out of the computational and physical domains. Discretizing the radiation condition (49) gives only one of these unknowns, $(p_{sc})_{i,n_2+1}^n$. For this reason it is necessary to use a 3-point approximation for $(p_{sc})_{\xi\eta}$ which is backwards in the variable η. Also the coordinate values of x_{i,n_2+1} and y_{i,n_2+1} are not defined so new approximations for x_η and y_η are

32
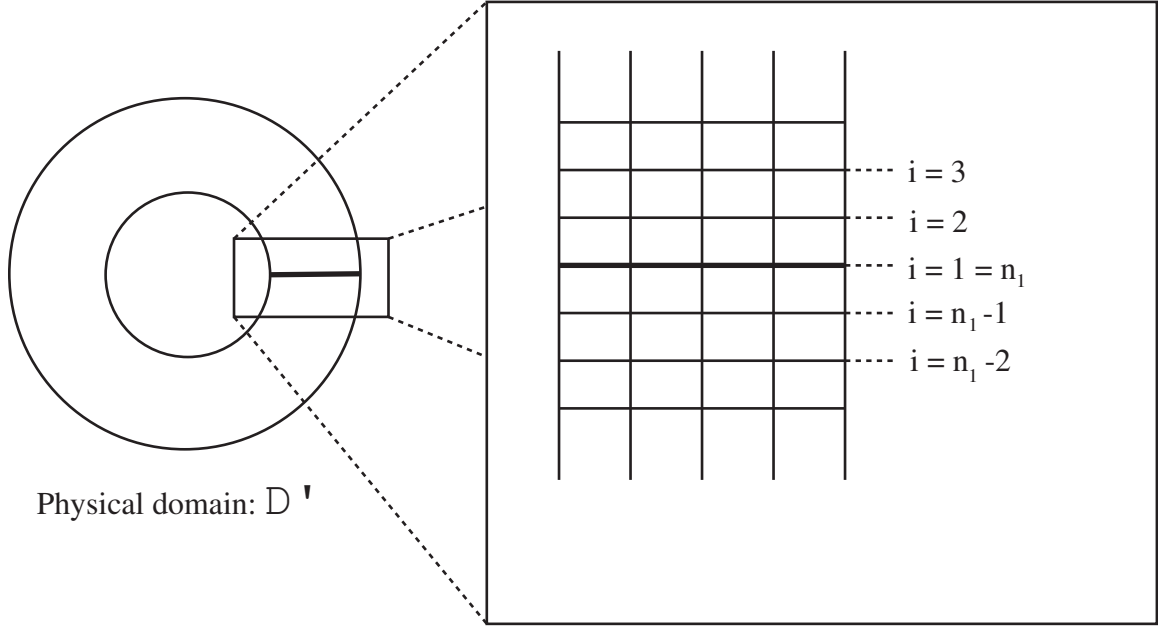
Figure 17: The physical domain at the branch cut indexed by points from the computational domain

needed which are also backwards in the direction of η. Along the outermost ring we use the alternative finite difference approximations for $(p_{sc})_{\xi\eta}$, x_η, and y_η

$$(p_{sc})_{\xi\eta} = \frac{1}{4}\Big(3(p_{sc})^n_{i+1,n_2} - 4(p_{sc})^n_{i+1,n_2-1} + (p_{sc})^n_{i+1,n_2-2} - 3(p_{sc})^n_{i-1,n_2}$$
$$+ 4(p_{sc})^n_{i-1,n_2-1} - (p_{sc})^n_{i-1,n_2-2}\Big) + \mathcal{O}(\Delta\xi\Delta\eta)$$
$$x_\eta = \frac{3}{2}x_{i,n_2} - 2x_{i,n_2-1} + \frac{1}{2}x_{i,n_2-2} + \mathcal{O}(\Delta\eta^2)$$
$$y_\eta = \frac{3}{2}y_{i,n_2} - 2y_{i,n_2-1} + \frac{1}{2}y_{i,n_2-2} + \mathcal{O}(\Delta\eta^2)$$

These alternate approximations are used to discretize the PDE (44). In order to discretize the radiation condition (49), the following finite difference approximations

33

for $(p_{sc})_t$, $(p_{sc})_\xi$, and $(p_{sc})_\eta$ are used:

$$(p_{sc})_t = \frac{1}{2\Delta t}\Big((p_{sc})^{n+1}_{i,n_2} - (p_{sc})^{n-1}_{i,n_2}\Big) + \mathcal{O}(\Delta t^2)$$

$$(p_{sc})_\xi = \frac{1}{2}\Big((p_{sc})^{n}_{i+1,n_2} - (p_{sc})^{n}_{i-1,n_2}\Big) + \mathcal{O}(\Delta\xi^2)$$

$$(p_{sc})_\eta = \frac{1}{2}\Big((p_{sc})^{n}_{i,n_2+1} - (p_{sc})^{n}_{i,n_2-1}\Big) + \mathcal{O}(\Delta\eta^2)$$

A single equation for $(p_{sc})^{n+1}_{i,n_2}$ can be obtained by solving the discretization of the radiation condition for $(p_{sc})^{n}_{i,n_2+1}$, plugging it into the discretization for the PDE (44) and solving it for $(p_{sc})^{n+1}_{i,n_2}$. The resulting discrete equation is given by

$$(p_{sc})^{n+1}_{i,n_2} = \frac{1}{1+\sigma}\Bigg\{2\Big[1 - \delta^2\Big(\alpha + \gamma + \frac{\gamma J}{2\kappa}\Big)\Big](p_{sc})^{n}_{i,n_2} \tag{51}$$
$$+ \delta^2\Big(\alpha + \frac{3\beta}{2} + \frac{\gamma\lambda}{\kappa}\Big)(p_{sc})^{n}_{i-1,n_2} + \delta^2\Big(\alpha - \frac{3\beta}{2} - \frac{\gamma\lambda}{\kappa}\Big)(p_{sc})^{n}_{i+1,n_2}$$
$$- \frac{\delta^2\beta}{2}\Big(4(p_{sc})^{n}_{i-1,n_2-1} - 4(p_{sc})^{n}_{i+1,n_2-1} + (p_{sc})^{n}_{i+1,n_2-2} - (p_{sc})^{n}_{i-1,n_2-2}\Big)$$
$$+ 2\delta^2\gamma(p_{sc})^{n}_{i,n_2-1} + (\sigma - 1)(p_{sc})^{n-1}_{i,n_2}\Bigg\},$$

for $1 \le i \le n_1$ and where $\delta = c\Delta t/J$ and $\sigma = \delta\gamma r_\infty/\kappa$. Equation (51) is not dependent on any points outside of the physical domain and is therefore used to determine the value of the scattered wave for all outer edge points with the same continuity modifications at the branch cut as used for the interior points.

This completes the computations over the entire computational domain $i = 1, 2, \ldots, n_1$ and $j = 1, 2, \ldots, n_2$ for one level in time. Levels in time are computed for $n = 1, 2, \ldots$ until the max point-wise difference between 2 successive levels in time fall below a specified tolerance ϵ. This uniform convergence is expressed as

$$\underset{i,j}{\text{Max}}\Big| |(p_{sc})^{n}_{i,j}| - |(p_{sc})^{n-1}_{i,j}| \Big| < \epsilon. \tag{52}$$

34

Figure 18: Comparison of Numerical Solution computed on a Winslow grid using the 3-point scheme with 131 rays and 101 rings to Analytical Solution for $\theta = \pi/6$ and Comparison of scattering cross sections
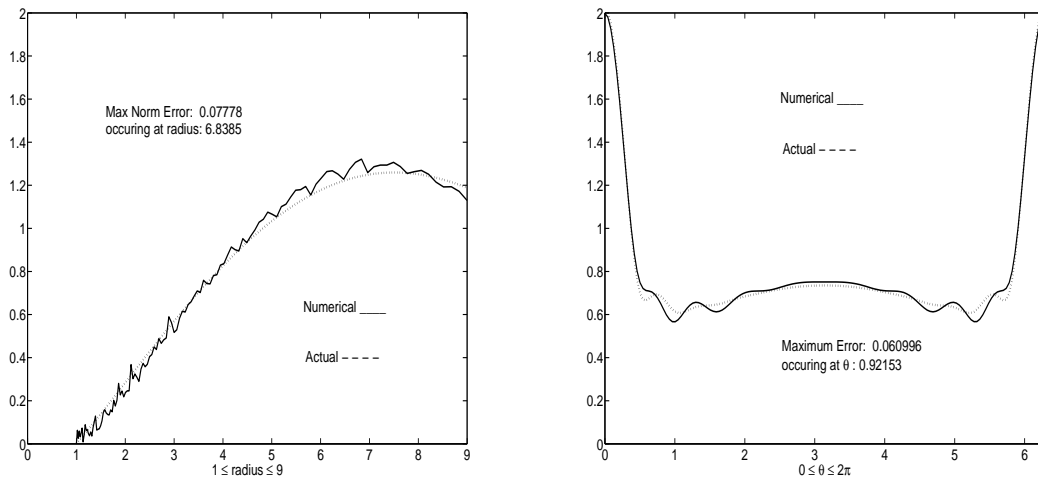
Figure 19: Comparison of Numerical Solution computed on a Winslow grid using the 3-point scheme with 151 rays and 121 rings to Analytical Solution for $\theta = \pi/6$ and Comparison of scattering cross sections

In summary, equations (50) and (51) are used together as we march in time to approximate the harmonic steady state of the scattered wave p_{sc}. This is done using 3-point finite difference approximations. We improve this to a 5-point scheme in the
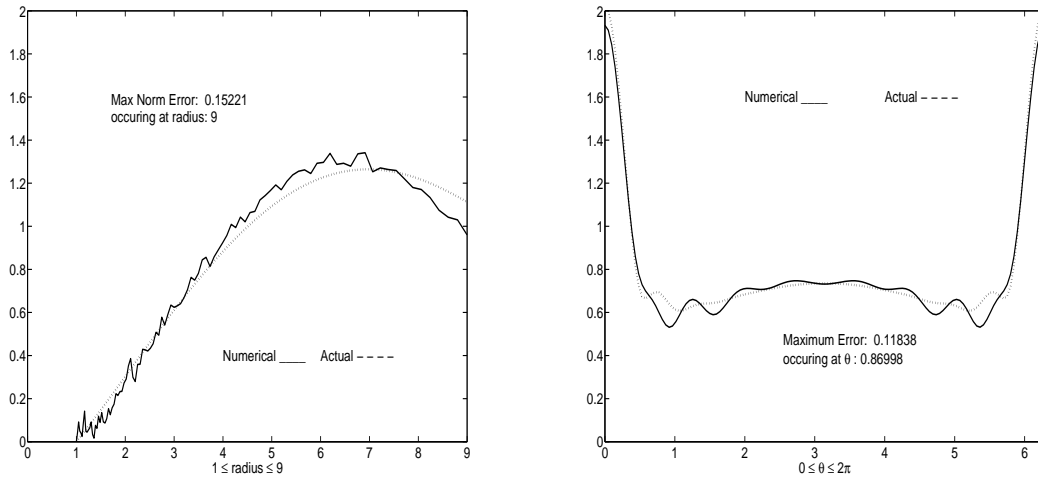
35
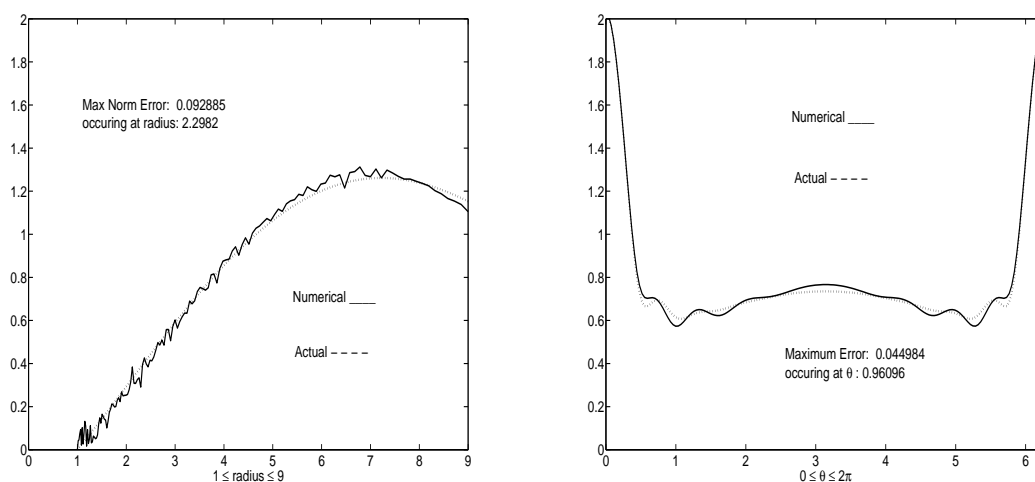
Figure 20: Comparison of Numerical Solution computed on a Winslow grid using the 3-point scheme with 171 rays and 141 rings to Analytical Solution for $\theta = \pi/6$ and Comparison of scattering cross sections

next section.

4.1.1 Results Using 3-Point Scheme

To determine the accuracy of the numerical solution using a 3-point scheme we compare the numerical solution for a circular boundary found using a Winslow grid to the analytical solution. This can only be done for circular boundaries because analytical solutions are not known for boundaries of arbitrary shape. First we set out to determine a grid size which yields desirable results. Grids with too few rays and rings led to inaccurate approximations. We didn't start to achieve convergence of the numerical solution to the analytical solution until we used grid sizes with around 100 rays and rings. Fig. (18) shows a comparison of the analytical solution to our numerical solution computed on a Winslow grid with 131 rays and 101 rings. The comparison is made along the ray at an angle of $\theta = \pi/6$ from the x-axis. In the same figure is a comparison of the scattering cross section of the numerical solution against that of the analytical solution. Similar comparisons are made in Fig. (19)

36

and Fig. (20) for grid sizes of 151×121 and 171×141 respectively. It is readily seen that the most accurate grid sizes were 151×121 and 171×141 seen in Fig. (19) and Fig. (20). The difference between the two grid sizes is negligible and so we favor the smaller 151×121 grid for easier computation. Now that we have narrowed down the selection of appropriate grid sizes for accurate approximations we explore in greater detail and variety the numerical solutions on these grids.

We will vary the step size in time from $\Delta t = 0.0005$ to $\Delta t = 0.05$, and for each step size we will compare the numerical solution to the analytical solution over the entire physical domain. For each step size in time, both the numerical and analytical solutions are computed on the same Winlsow grid and then are compared by taking the absolute value of their point-wise differences. The maximum point-wise differences can be seen in the table in Fig. (21).

rays	rings	Δt	Max Difference with Analytical Solution	Location of Max Difference
151	121	0.0005	0.24821	$(8.7172 , \pm 2.2382)$
151	121	0.001	0.27201	$(8.6762 , 0.0000)$
151	121	0.005	0.32693	$(1.2686 , 0.0000)$
151	121	0.01	0.24967	$(1.2920 , 0.0000)$
151	121	0.05	no convergence	no convergence

Figure 21: Table comparing the accuracy of the Numerical Solution using the 3-point scheme for varying Δt

The data from the table in Fig. (21) would seem to indicate that varying the step size in time has minimal effect on the accuracy of the numerical solution as long as the time step resulted in a stable, convergent scheme. This is expected because of the limiting amplitude principle which states that with time the solution will approach a time harmonic steady state. We look at plots of the point-wise differences between numerical and analytical solutions near the boundary of the obstacle. Fig. (22) shows the 2 plots of the point-wise differences for both $\Delta t = 0.0005$ on the left and

37
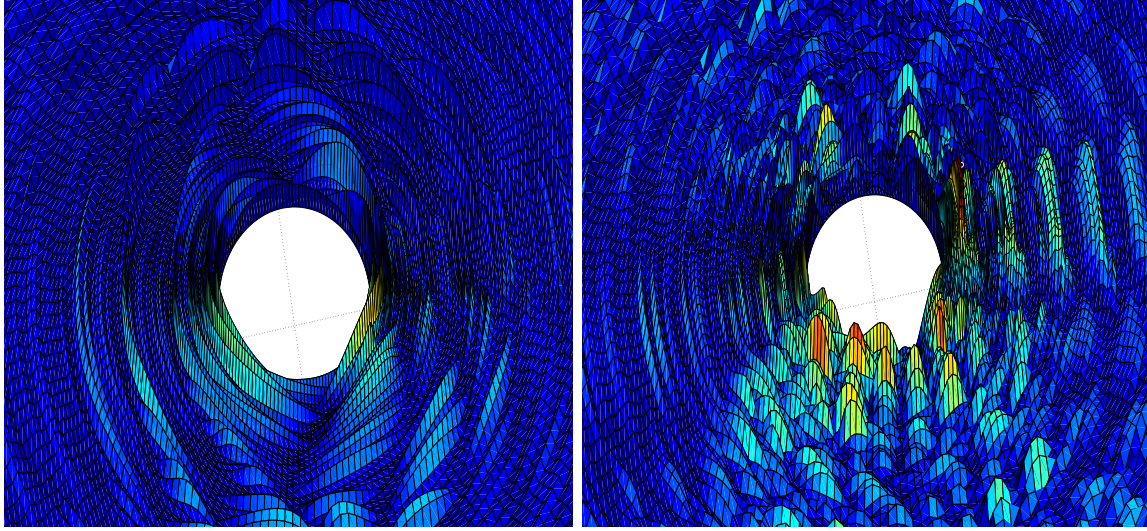
Figure 22: Comparison of plots, near the boundary of the obstacle, of the point-wise differences between the analytical and numerical solutions using the 3-point scheme on a 151×121 Winslow grid with $\Delta t = 0.0005$ on the left and $\Delta t = 0.01$ on the right

$\Delta t = 0.01$ on the right, both time steps resulting in convergent schemes. It is clear that the smaller step size produces a smoother and more stable approximation. This is because of the nature of the Winslow grid. Fig. (10) shows how Winslow grids are irregular in radius step sizes. The rings are tightly clustered near the boundary of the obstacle creating a finer mesh near the obstacle. For accuracy near the obstacle it is necessary to also have smaller step sizes in time. Near the obstacle, the step size of $\Delta t = 0.01$ is too large by comparison to the radius and angle step sizes giving a less smooth result while the step size $\Delta t = 0.05$ was simply too large for convergence. This implies that stability conditions exist but are unknown at present for arbitrary curvilinear coordinates. The plot of the numerical solution with 151 rays, 121 rings, and $\Delta t = 0.0005$ can be seen in Fig. (23). The average point-wise difference with the analytical solution is 0.029154 which is about a 1% error.
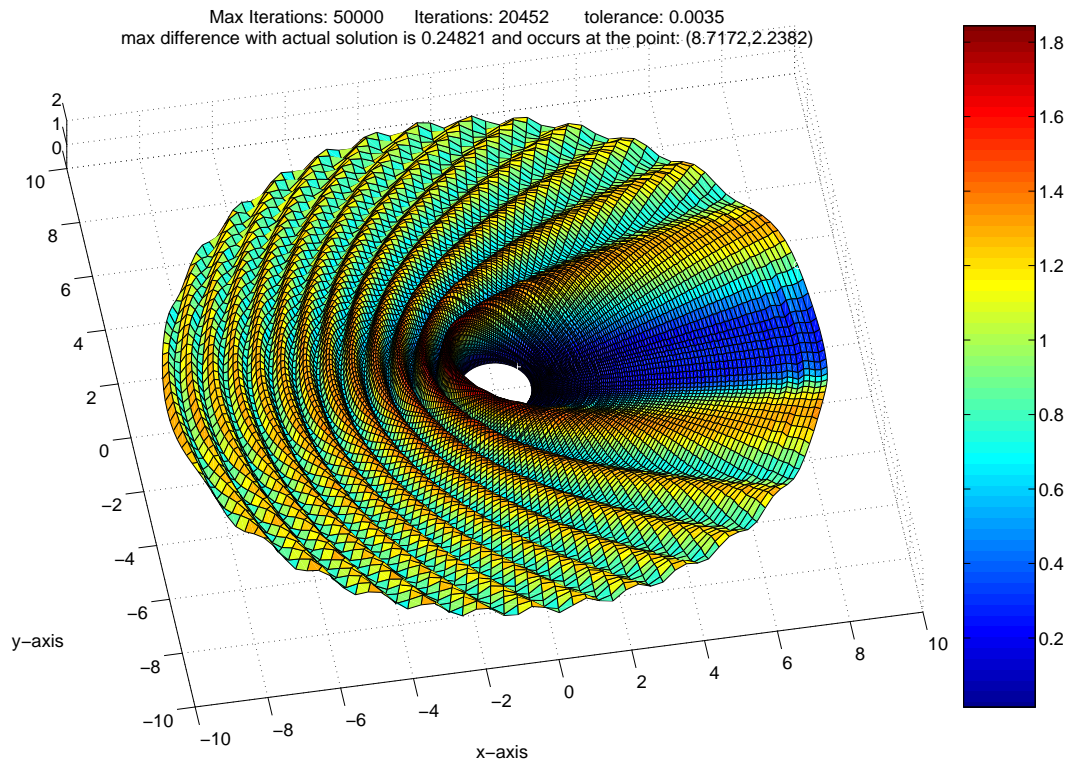
Figure 23: Numerical Solution using a 151×121 Winslow grid with $\Delta t = 0.0005$ using a 3-point scheme

The accuracy of the numerical solution using a Winslow grid with 151 rays, 121 rings, and $\Delta t = 0.0005$ serves as a basis for the accuracy of numerical solutions for arbitrarily shaped obstacles for which no analytical solution exists. First we approach the obstacle with 3-petal rose cross-section as seen in Fig. (25). The result is as expected with the shallow zone located directly behind the obstacle and the wave scattering symmetrically from the 2 petals facing the incoming incident wave. A more complicated scattering from a 4-petal rose is seen in Fig. (26) where the incoming wave scatters from 3 of the four petals. The scattering cross sections for both the 3-petal and 4-petal rose are shown in Fig. (24).
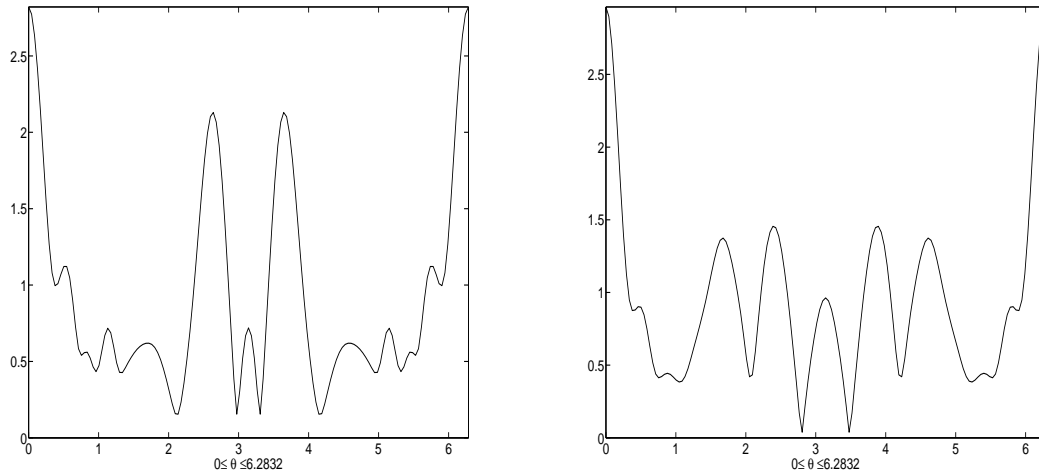
Figure 24: The scattering cross sections for the 3-petal rose on the left and the 4-petal rose on the right
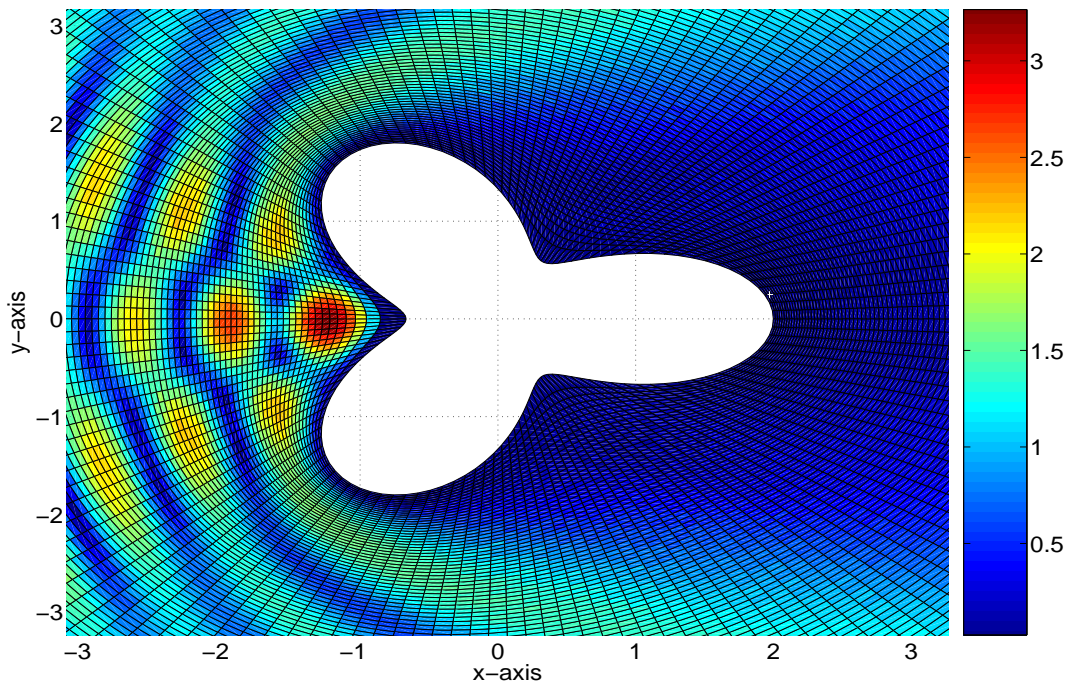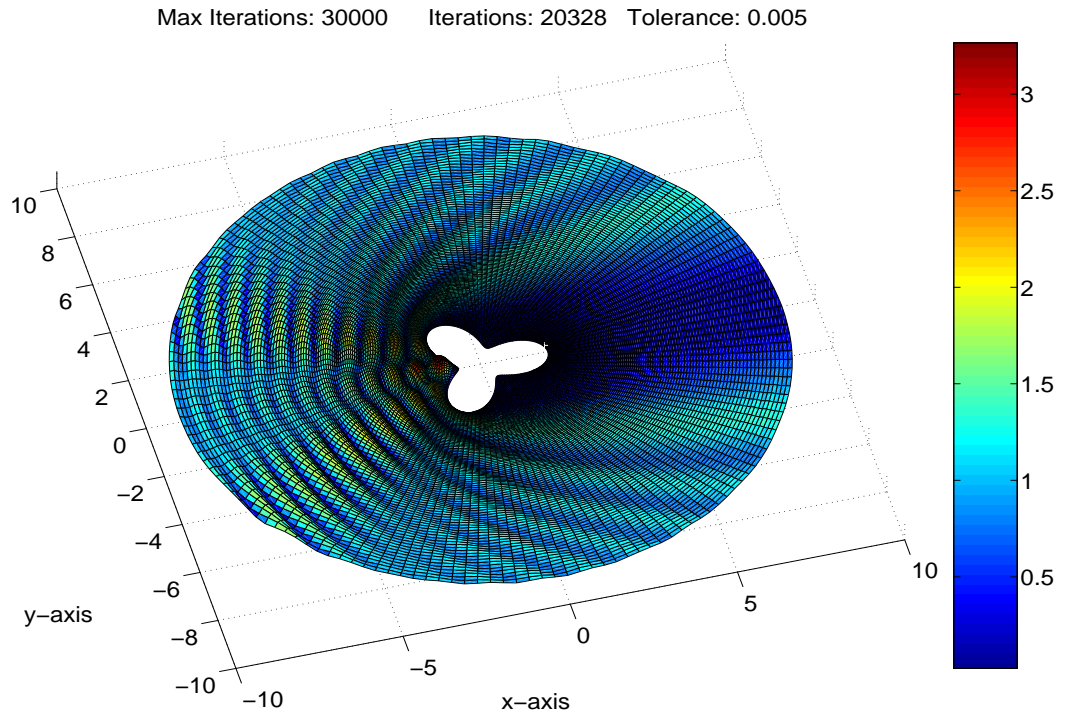
Figure 25: Numerical Solution with 3-petal rose cross-section using a 151×121 Winslow grid with $\Delta t = 0.0005$

41
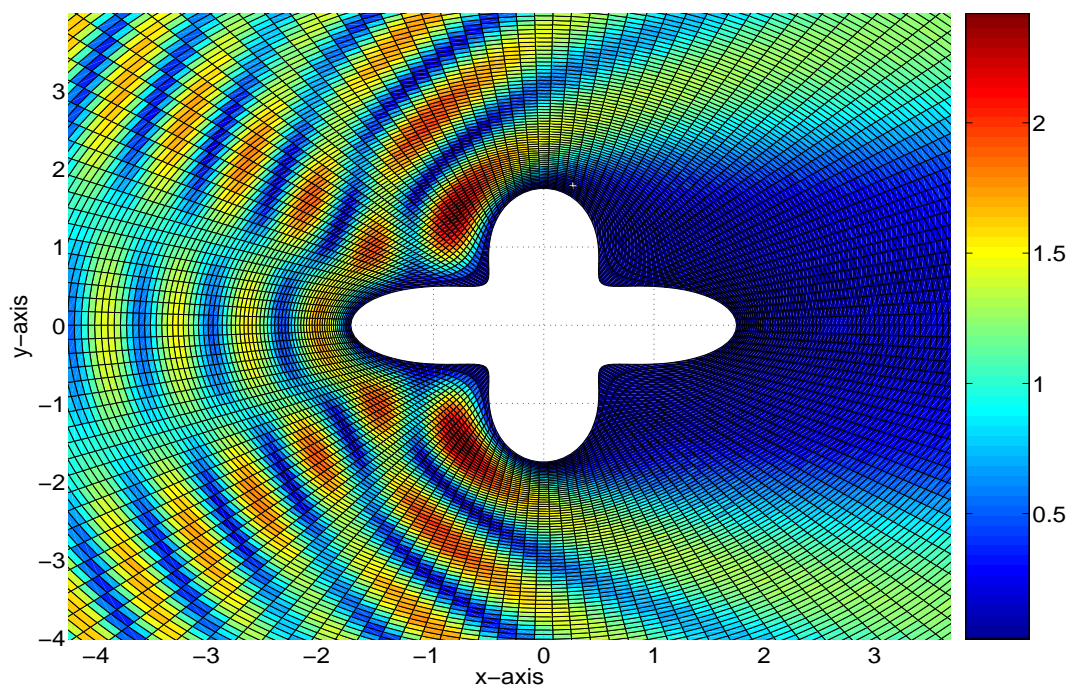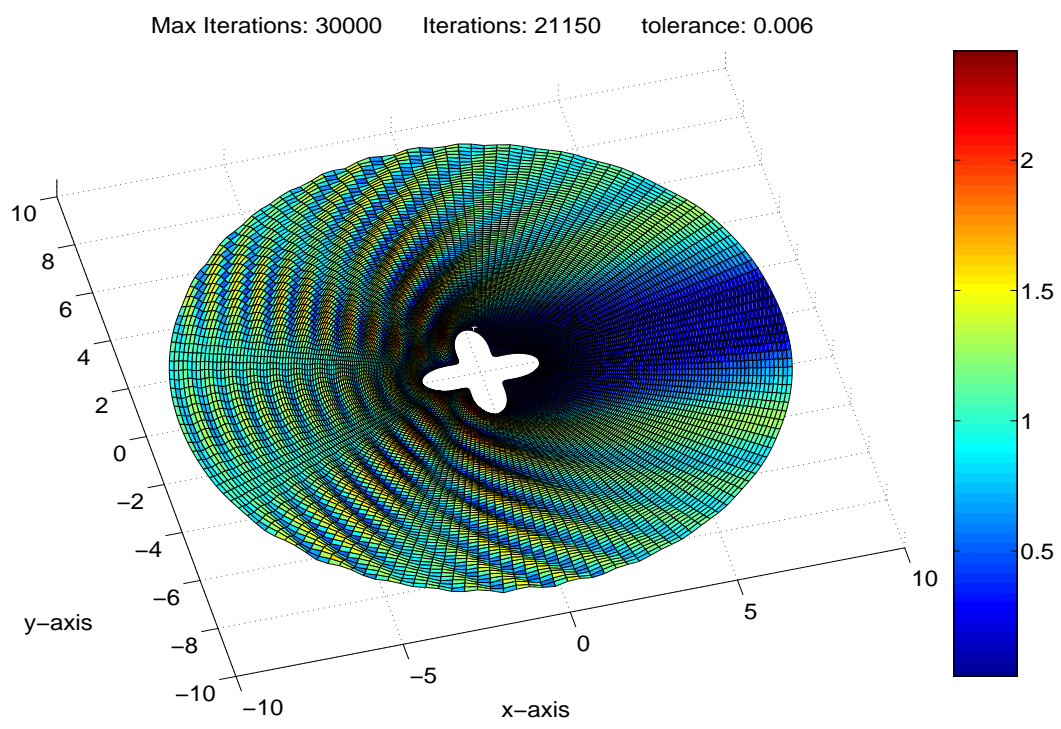
Figure 26: Numerical Solution with 4-petal rose cross-section using a 151×121 Winslow grid with $\Delta t = 0.0005$

We next look at the scattering from 2 obstacles of circular cross-section with notches cut out on the side of the obstacle facing the incoming wave. One obstacle has a pie shaped wedge cut out resulting in a cross-section which resembles pacman, as shown in Fig. (28). The other has a circular notch removed which gives a cross-section in the shape of a crescent moon, as shown in Fig. (29). These figures show the scattering to be symmetric. This is as expected and is due to the symmetry of the cross-sections with respect to the direction of the incoming wave. The scattering cross sections are shown in Fig. (27).
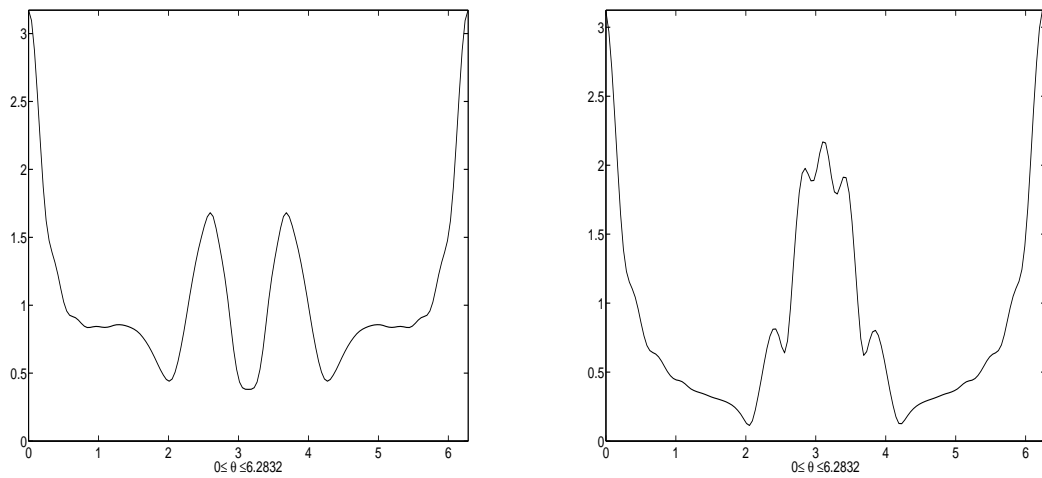
Figure 27: The scattering cross sections for the pacman on the left and the crescent on the right

43
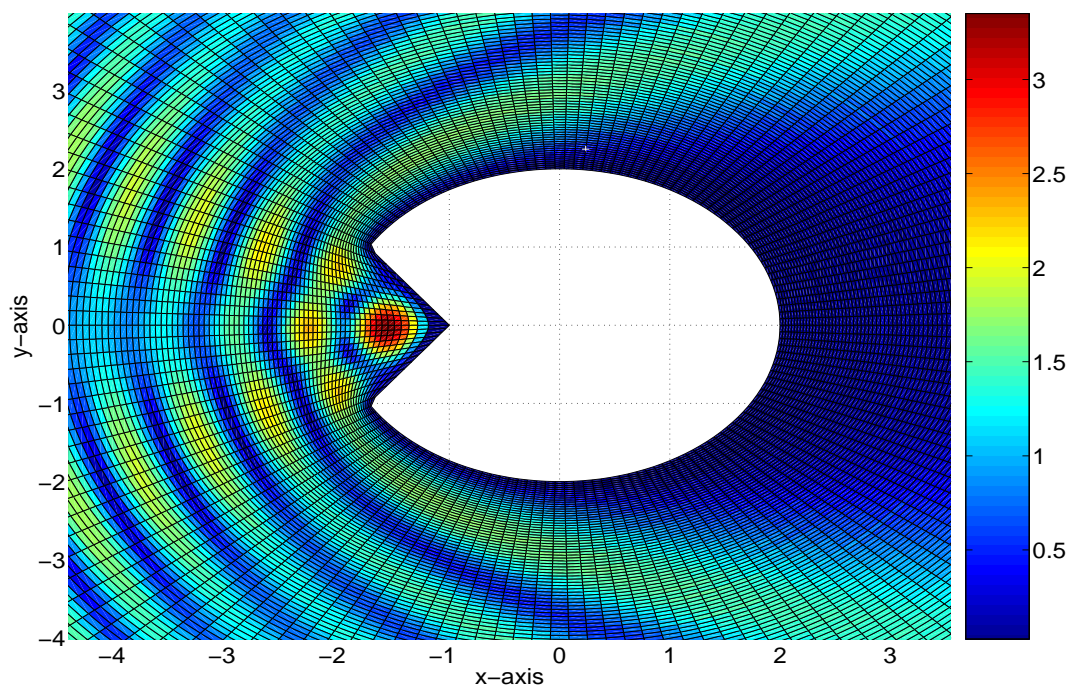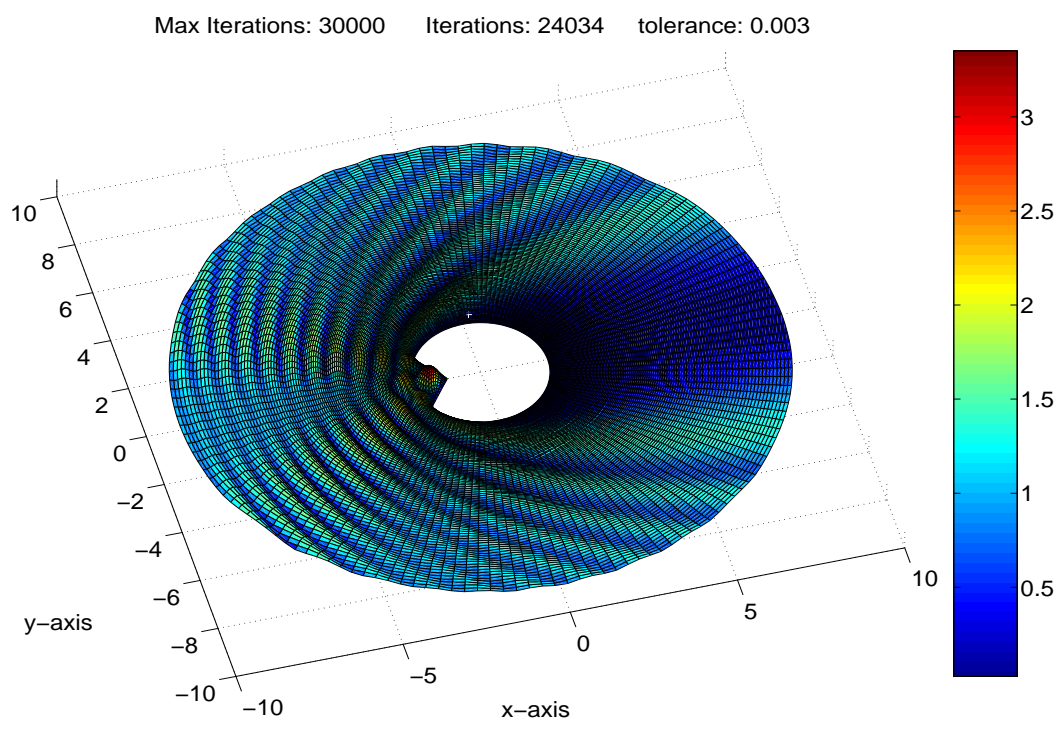
Figure 28: Numerical Solution with pacman cross-section using a 151×121 Winslow grid with $\Delta t = 0.0005$

44

Max Iterations: 30000   Iterations: 27798   tolerance: 0.005
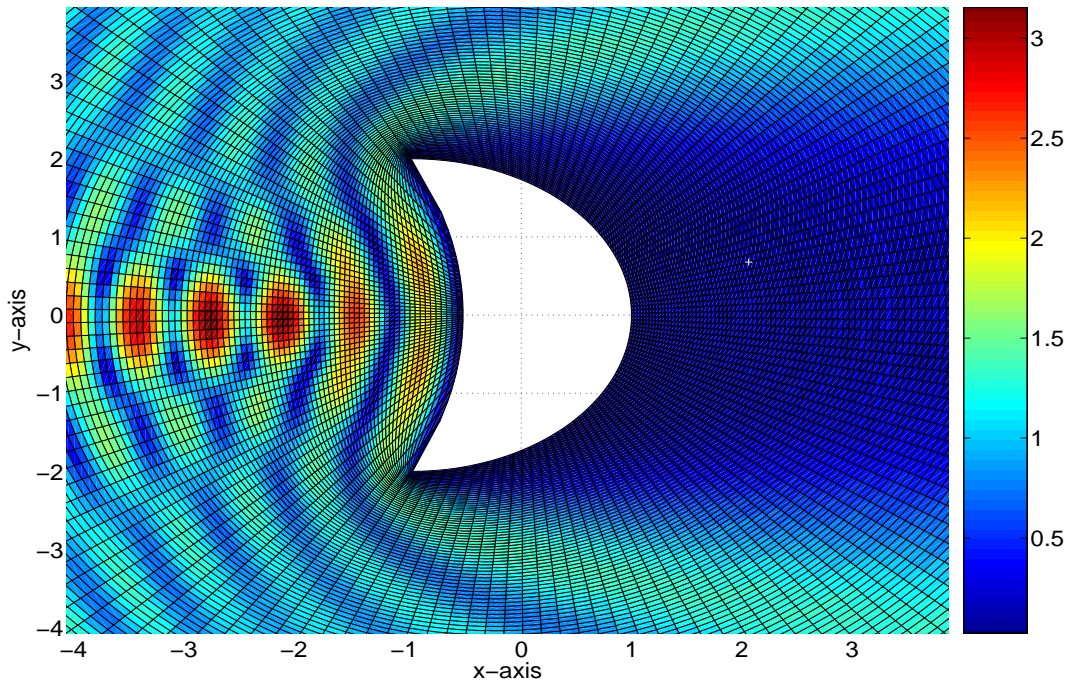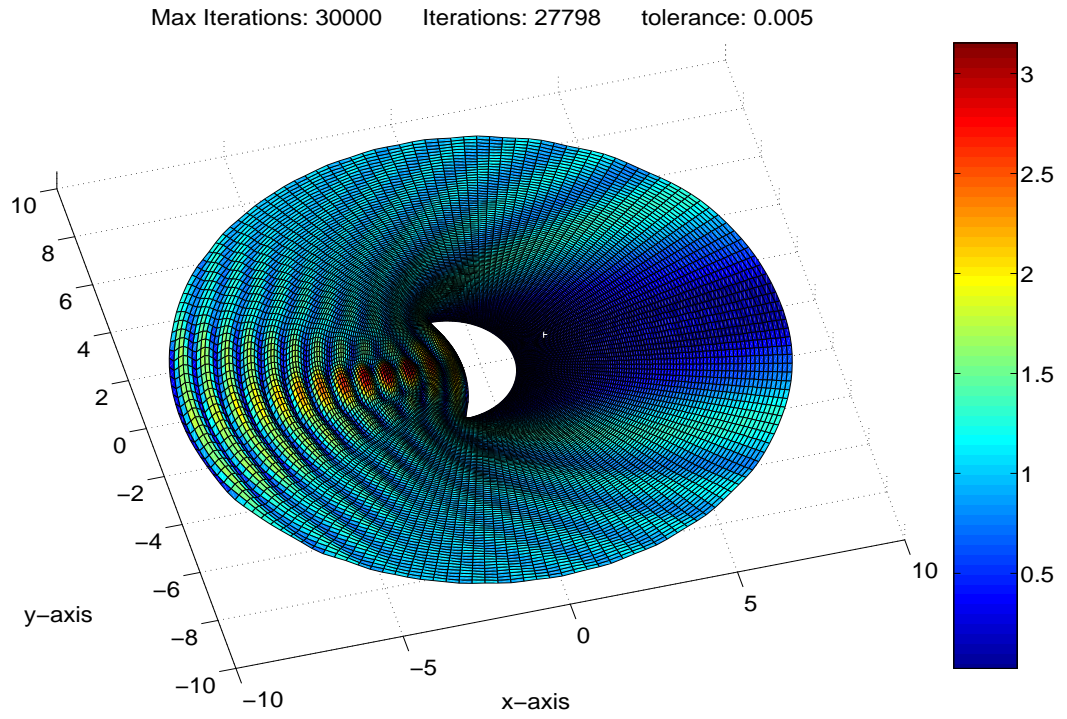
Figure 29: Numerical Solution with crescent cross-section using a 151×121 Winslow grid with $\Delta t = 0.0005$

It is of interest to also study the scattering from obstacles of geometric cross-section. The scattering from a circular cross-section has been fully developed. We now approximate the scattering of the incoming incident wave by obstacles of triangular and rectangular cross-sections, as shown in Fig. (32) and Fig. (31). The results are as expected with the scattering of the wave depicting a reflection by the straight surfaces of the obstacle facing the incoming wave. The scattering cross sections are shown in Fig. (30).
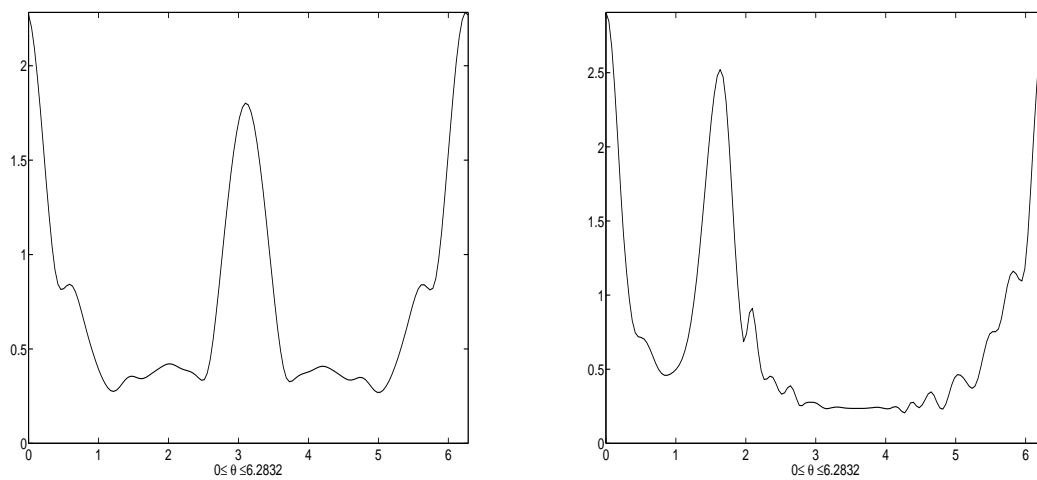
Figure 30: The scattering cross sections for the square on the left and triangle on the right

46
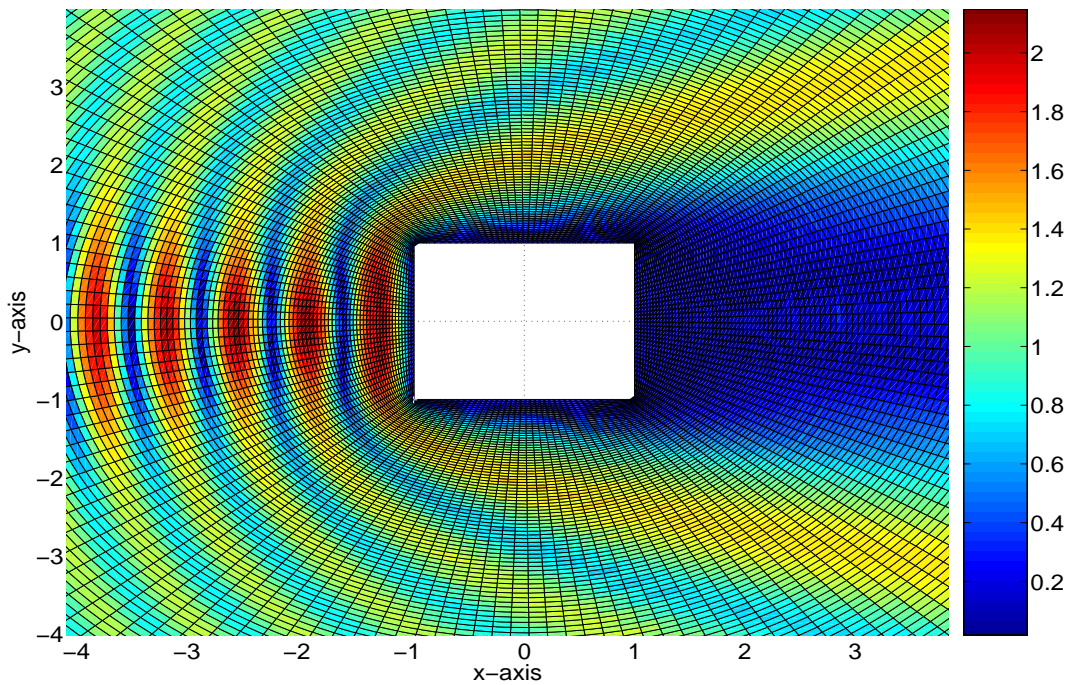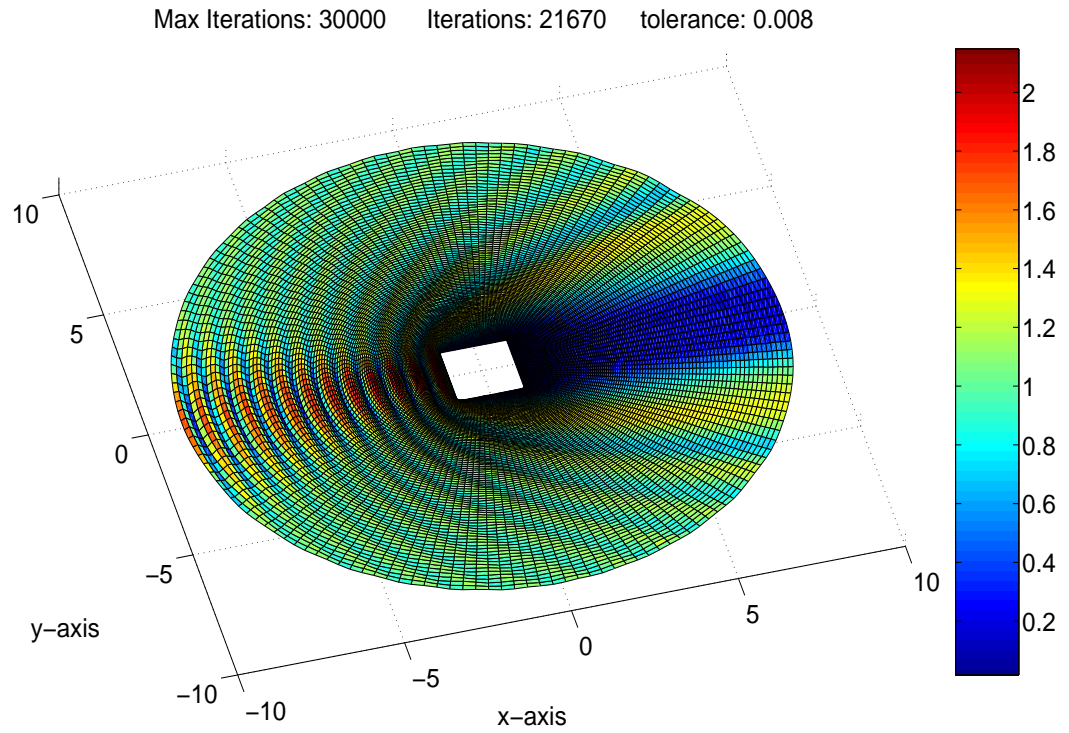
Figure 31: Numerical Solution with square cross-section using a 151×121 Winslow grid with $\Delta t = 0.0005$

Max Iterations: 30000   Iterations: 21582   tolerance: 0.012
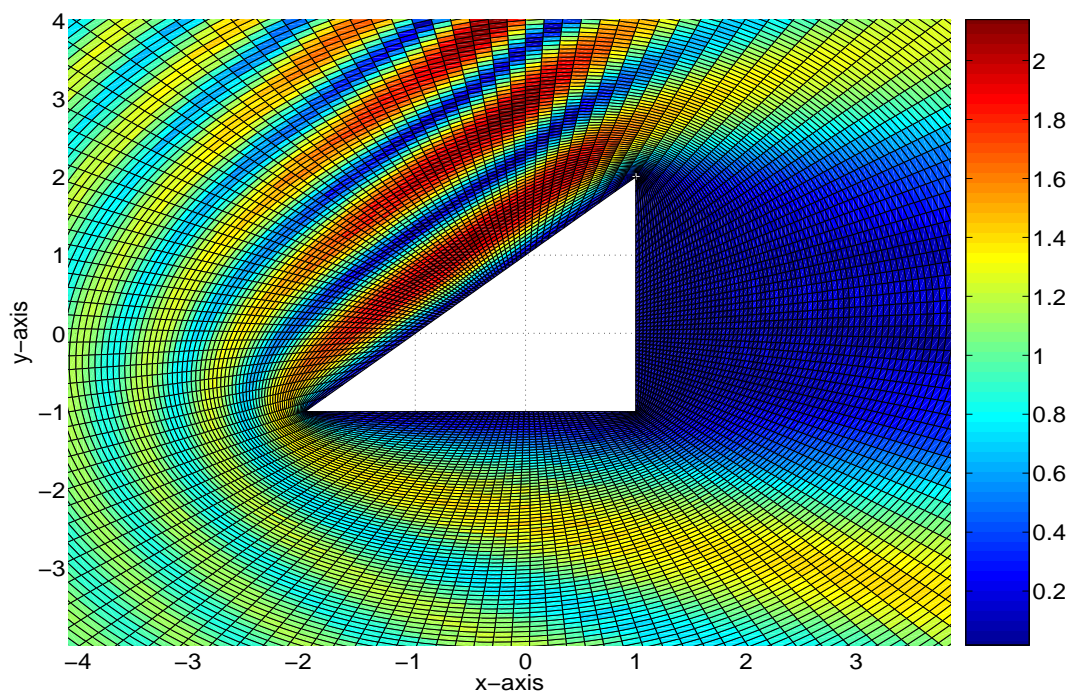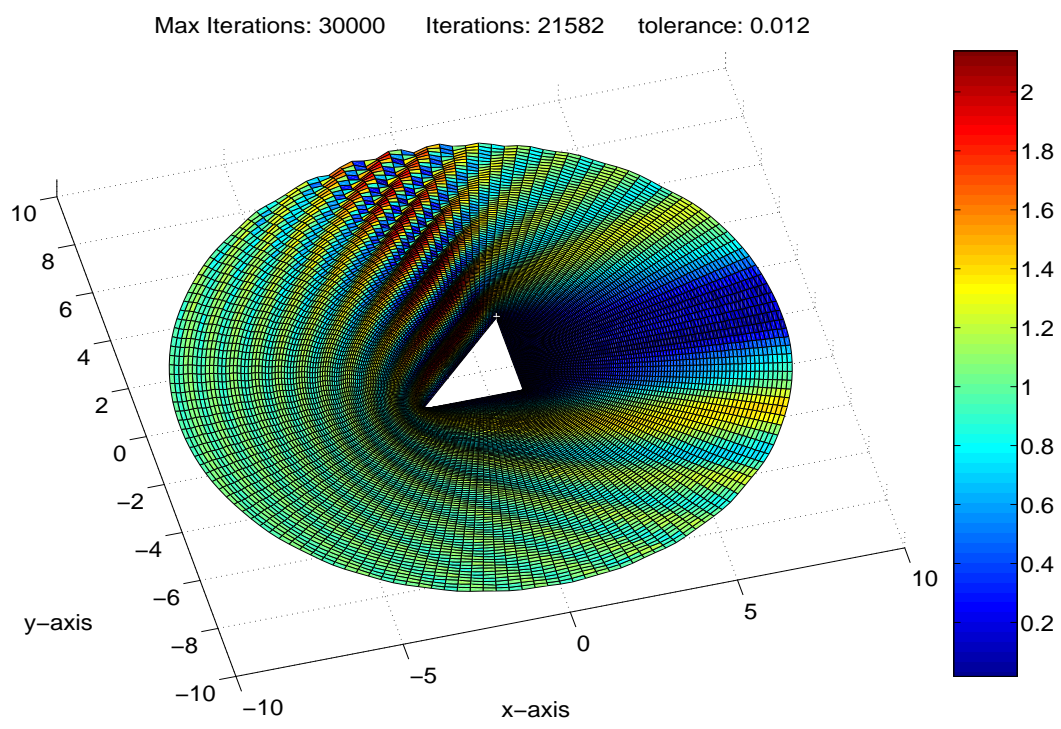
Figure 32: Numerical Solution with triangle cross-section using a 151×121 Winslow grid with $\Delta t = 0.0005$

4.2 Higher Order 5-Point Scheme

In an effort to generate more accurate solutions we decided to use higher order 5-point finite difference approximations for the derivatives in the directions of ξ and η and the same 3-point scheme as before for the time derivatives. These schemes will be used to numerically solve the PDE (44). In order to not leave the physical domain, we will require the use of a variety of finite difference equations to approximate p_{sc} depending on which region is being computed. Like for the 3-point scheme, the initial conditions give $p_{sc} = 0$, except at the boundary, for the first time level, $n = 1$. So we start our computations at the second level. Because we are still using a centered 3-point scheme for the derivative with respect to time t, to compute any level in time requires data from the previous two levels in time. To compute the second level in time we need to impose a ghost level which precedes the first level and which has the condition $p_{sc} = 0$.

For the boundary of the obstacle, $j = 1$, we use the boundary condition (48) $p_{sc} = -p_{inc}$ as usual. For the second ring, $j = 2$, derivatives in the direction of η must be approximated using a non-centered 5-point scheme indexed from 1 up to 5. This way we won't have points outside of the physical domain. For the time derivatives and the derivatives in the direction of ξ, we use the regular centered 3-point and 5-point schemes respectively. For the scale metric factors α, β and γ we use the following finite differences:

$$x_\xi = \frac{1}{12}\Big(x_{i-2,2} - 8x_{i-1,2} + 8x_{i+1,2} - x_{i+2,2}\Big) + \mathcal{O}(\Delta\xi^4)$$
$$x_\eta = \frac{1}{12}\Big(-3x_{i,1} - 10x_{i,2} + 18x_{i,3} - 6x_{i,4} + x_{i,5}\Big) + \mathcal{O}(\Delta\eta^4)$$
$$y_\xi = \frac{1}{12}\Big(y_{i-2,2} - 8y_{i-1,2} + 8y_{i+1,2} - y_{i+2,2}\Big) + \mathcal{O}(\Delta\xi^4)$$
$$y_\eta = \frac{1}{12}\Big(-3y_{i,1} - 10y_{i,2} + 18y_{i,3} - 6y_{i,4} + y_{i,5}\Big) + \mathcal{O}(\Delta\eta^4),$$

49

for $1 \leq i \leq n_1$. Finite difference approximations for the other derivative in the PDE (44) are given by

$$(p_{sc})_{tt} = \frac{1}{\Delta t^2}\Big((p_{sc})_{i,2}^{n+1} - 2(p_{sc})_{i,2}^n + (p_{sc})_{i,2}^{n-1}\Big) + \mathcal{O}(\Delta t^2)$$

$$(p_{sc})_{\xi\xi} = \frac{1}{12}\Big(-(p_{sc})_{i-2,2}^n + 16(p_{sc})_{i-1,2}^n - 30(p_{sc})_{i,2}^n$$
$$+ 16(p_{sc})_{i+1,2}^n - (p_{sc})_{i+2,2}^n\Big) + \mathcal{O}(\Delta\xi^4)$$

$$(p_{sc})_{\eta\eta} = \frac{1}{12}\Big(11(p_{sc})_{i,1}^n - 20(p_{sc})_{i,2}^n + 6(p_{sc})_{i,3}^n$$
$$+ 4(p_{sc})_{i,4}^n - (p_{sc})_{i,5}^n\Big) + \mathcal{O}(\Delta\eta^4)$$

$$(p_{sc})_{\xi\eta} = \frac{1}{144}\Big[-3\Big((p_{sc})_{i-2,1}^n - 8(p_{sc})_{i-1,1}^n + 8(p_{sc})_{i+1,1}^n - (p_{sc})_{i+2,1}^n\Big)$$
$$- 10\Big((p_{sc})_{i-2,2}^n - 8(p_{sc})_{i-1,2}^n + 8(p_{sc})_{i+1,2}^n - (p_{sc})_{i+2,2}^n\Big)$$
$$+ 18\Big((p_{sc})_{i-2,3}^n - 8(p_{sc})_{i-1,3}^n + 8(p_{sc})_{i+1,3}^n - (p_{sc})_{i+2,3}^n\Big)$$
$$- 6\Big((p_{sc})_{i-2,4}^n - 8(p_{sc})_{i-1,4}^n + 8(p_{sc})_{i+1,4}^n - (p_{sc})_{i+2,4}^n\Big)$$
$$+ \Big((p_{sc})_{i-2,5}^n - 8(p_{sc})_{i-1,5}^n + 8(p_{sc})_{i+1,5}^n - (p_{sc})_{i+2,5}^n\Big)\Big] + \mathcal{O}(\Delta\xi^2\Delta\eta^2).$$

Plugging these into the PDE (44) and solving for $(p_{sc})_{i,2}^{n+1}$, we get

$$
\begin{aligned}
(p_{sc})_{i,2}^{n+1} = &\left(2 - \frac{5\delta^2\alpha}{2} - \frac{5\delta^2\gamma}{3}\right)(p_{sc})_{i,2}^n \qquad\qquad\qquad (53)\\
&+ \delta^2\left(\frac{5\beta}{36} - \frac{\alpha}{12}\right)(p_{sc})_{i-2,2}^n + \delta^2\left(\frac{4\alpha}{3} - \frac{10\beta}{9}\right)(p_{sc})_{i-1,2}^n\\
&+ \delta^2\left(\frac{4\alpha}{3} + \frac{10\beta}{9}\right)(p_{sc})_{i+1,2}^n + \delta^2\left(-\frac{5\beta}{36} - \frac{\alpha}{12}\right)(p_{sc})_{i+2,2}^n\\
&- \frac{\delta^2\beta}{72}\Bigg[-3\Big((p_{sc})_{i-2,1}^n - 8(p_{sc})_{i-1,1}^n + 8(p_{sc})_{i+1,1}^n - (p_{sc})_{i+2,1}^n\Big)\\
&+ 18\Big((p_{sc})_{i-2,2}^n - 8(p_{sc})_{i-1,2}^n + 8(p_{sc})_{i+1,2}^n - (p_{sc})_{i+2,2}^n\Big)\\
&- 6\Big((p_{sc})_{i-2,3}^n - 8(p_{sc})_{i-1,3}^n + 8(p_{sc})_{i+1,3}^n - (p_{sc})_{i+2,3}^n\Big)\\
&+ \Big((p_{sc})_{i-2,4}^n - 8(p_{sc})_{i-1,4}^n + 8(p_{sc})_{i+1,4}^n - (p_{sc})_{i+2,4}^n\Big)\Bigg]\\
&+ \frac{\delta^2\gamma}{12}\Big(11(p_{sc})_{i,1}^n + 6(p_{sc})_{i,3}^n + 4(p_{sc})_{i,4}^n - (p_{sc})_{i,5}^n\Big) - (p_{sc})_{i,2}^{n-1},
\end{aligned}
$$

for $1 \leq i \leq n_1$ and where $\delta = c\Delta t/J$. Using equations (48) and (53) we can compute $(p_{sc})_{i,j}^{n+1}$ for the first two rings for which we will need to impose continuity conditions along the branch cut. Because we are using a 5-point scheme, this will be a little more complicated than before. When $i = 1$ the value of $(p_{sc})_{i-2,2}^n = (p_{sc})_{-1,2}^n$ and $(p_{sc})_{i-1,2}^n = (p_{sc})_{0,2}^n$ in equation (53) are determined by instead using their respective physical equivalents $(p_{sc})_{i,n_1-2}^n$ and $(p_{sc})_{n_1-1,2}^n$. When $i = 2$ the value of $(p_{sc})_{i-2,2}^n = (p_{sc})_{0,2}^n$ in equation (53) is determined by instead using its physical equivalent $(p_{sc})_{n_1-1,2}^n$. When $i = n_1 - 1$ the value of $(p_{sc})_{i+2,2}^n = (p_{sc})_{n_1+1,2}^n$ in equation (53) is determined by instead using its physical equivalent $(p_{sc})_{2,2}^n$. When $i = n_1$ the value of p_{sc} is set equal to its value for $i = 1$ to avoid the computation of p_{sc} over the same physical point. These correlations between indices $i = -1$ and $i = n_1 - 2$, indices $i = 0$ and $i = n_1 - 1$, and indices $i = 1$ and $i = n_1 + 1$ can be seen in Fig. (17). Similar replacements are made for the approximations of the derivatives in the direction of ξ for the coordinates x

51

and y. We now consider the computation of the interior.

For the interior, $j = 3, 4, \ldots, n_2 - 2$ and $1 \leq i \leq n_1$, we can use centered 5-point finite differences without ever leaving the physical domain. For the scale metric factors α, β and γ we use the following finite differences:

$$x_\xi = \frac{1}{12}\Big(x_{i-2,j} - 8x_{i-1,j} + 8x_{i+1,j} - x_{i+2,j}\Big) + \mathcal{O}(\Delta\xi^4)$$

$$x_\eta = \frac{1}{12}\Big(x_{i,j-2} - 8x_{i,j-1} + 8x_{i,j+1} - x_{i,j+2}\Big) + \mathcal{O}(\Delta\eta^4)$$

$$y_\xi = \frac{1}{12}\Big(y_{i-2,j} - 8y_{i-1,j} + 8y_{i+1,j} - y_{i+2,j}\Big) + \mathcal{O}(\Delta\xi^4)$$

$$y_\eta = \frac{1}{12}\Big(y_{i,j-2} - 8y_{i,j-1} + 8y_{i,j+1} - y_{i,j+2}\Big) + \mathcal{O}(\Delta\eta^4)$$

Finite difference approximations for the other derivative in the PDE (44) are given by

$$(p_{sc})_{tt} = \frac{1}{\Delta t^2}\Big((p_{sc})_{i,j}^{n+1} - 2(p_{sc})_{i,j}^n + (p_{sc})_{i,j}^{n-1}\Big) + \mathcal{O}(\Delta t^2)$$

$$(p_{sc})_{\xi\xi} = \frac{1}{12}\Big(-(p_{sc})_{i-2,j}^n + 16(p_{sc})_{i-1,j}^n - 30(p_{sc})_{i,j}^n$$

$$+ 16(p_{sc})_{i+1,j}^n - (p_{sc})_{i+2,j}^n\Big) + \mathcal{O}(\Delta\xi^4)$$

$$(p_{sc})_{\eta\eta} = \frac{1}{12}\Big(-(p_{sc})_{i,j-2}^n + 16(p_{sc})_{i,j-1}^n - 30(p_{sc})_{i,j}^n$$

$$+ 16(p_{sc})_{i,j+1}^n - (p_{sc})_{i,j+2}^n\Big) + \mathcal{O}(\Delta\eta^4)$$

$$(p_{sc})_{\xi\eta} = \frac{1}{144}\bigg[\Big((p_{sc})_{i-2,j-2}^n - 8(p_{sc})_{i-1,j-2}^n + 8(p_{sc})_{i+1,j-2}^n - (p_{sc})_{i+2,j-2}^n\Big)$$

$$- 8\Big((p_{sc})_{i-2,j-1}^n - 8(p_{sc})_{i-1,j-1}^n + 8(p_{sc})_{i+1,j-1}^n - (p_{sc})_{i+2,j-1}^n\Big)$$

$$+ 8\Big((p_{sc})_{i-2,j+1}^n - 8(p_{sc})_{i-1,j+1}^n + 8(p_{sc})_{i+1,j+1}^n - (p_{sc})_{i+2,j+1}^n\Big)$$

$$- \Big((p_{sc})_{i-2,j+2}^n - 8(p_{sc})_{i-1,j+2}^n + 8(p_{sc})_{i+1,j+2}^n$$

$$- (p_{sc})_{i+2,j+2}^n\Big)\bigg] + \mathcal{O}(\Delta\xi^2\Delta\eta^2).$$

After substituting them into the PDE (44) and solving for $(p_{sc})_{i,j}^{n+1}$, we get

$$
\begin{aligned}
(p_{sc})_{i,j}^{n+1} = &\left(2 - \frac{5\delta^2\alpha}{2} - \frac{5\delta^2\gamma}{2}\right)(p_{sc})_{i,j}^n \qquad\qquad\qquad (54)\\
&+ \frac{\delta^2\alpha}{12}\Big(-(p_{sc})_{i-2,j}^n + 16(p_{sc})_{i-1,j}^n + 16(p_{sc})_{i+1,j}^n - (p_{sc})_{i+2,j}^n\Big)\\
&- \frac{\delta^2\beta}{72}\Bigg[\Big((p_{sc})_{i-2,j-2}^n - 8(p_{sc})_{i-1,j-2}^n + 8(p_{sc})_{i+1,j-2}^n - (p_{sc})_{i+2,j-2}^n\Big)\\
&\quad - 8\Big((p_{sc})_{i-2,j-1}^n - 8(p_{sc})_{i-1,j-1}^n + 8(p_{sc})_{i+1,j-1}^n - (p_{sc})_{i+2,j-1}^n\Big)\\
&\quad + 8\Big((p_{sc})_{i-2,j+1}^n - 8(p_{sc})_{i-1,j+1}^n + 8(p_{sc})_{i+1,j+1}^n - (p_{sc})_{i+2,j+1}^n\Big)\\
&\quad - \Big((p_{sc})_{i-2,j+2}^n - 8(p_{sc})_{i-1,j+2}^n + 8(p_{sc})_{i+1,j+2}^n - (p_{sc})_{i+2,j+2}^n\Big)\Bigg]\\
&+ \frac{\delta^2\gamma}{12}\Big(-(p_{sc})_{i,j-2}^n + 16(p_{sc})_{i,j-1}^n 16(p_{sc})_{i,j+1}^n - (p_{sc})_{i,j+2}^n\Big) - (p_{sc})_{i,j}^{n-1},
\end{aligned}
$$

for $3 \leq j \leq n_2 - 2$ and $1 \leq i \leq n_1$ and where $\delta = c\Delta t/J$. Using equation (54) we can compute p_{sc} for the interior. We impose the same continuity conditions along the branch cut as described for the second ring, $j = 2$. We now consider the computation of the second to last ring.

For the second to last ring, corresponding to the index $j = n_2 - 1$, derivatives in the direction of η must be approximated using a non-centered 5-point scheme indexed from $j = n_2 - 4$ up to $j = n_2$. This way we won't have points outside of the physical domain. For the time derivatives and the derivatives in the direction of ξ, we use the normal centered 3-point and 5-point schemes respectively. For the scale metric

53

factors α, β and γ we use

$$x_\xi = \frac{1}{12}\Big(x_{i-2,n_2-1} - 8x_{i-1,n_2-1} + 8x_{i+1,n_2-1} - x_{i+2,n_2-1}\Big) + \mathcal{O}(\Delta\xi^4)$$

$$x_\eta = \frac{1}{12}\Big(-x_{i,n_2-4} + 6x_{i,n_2-3} - 18x_{i,n_2-2} + 10x_{i,n_2-1} + 3x_{i,n_2}\Big) + \mathcal{O}(\Delta\eta^4)$$

$$y_\xi = \frac{1}{12}\Big(y_{i-2,n_2-1} - 8y_{i-1,n_2-1} + 8y_{i+1,n_2-1} - y_{i+2,n_2-1}\Big) + \mathcal{O}(\Delta\xi^4)$$

$$x_\eta = \frac{1}{12}\Big(-y_{i,n_2-4} + 6y_{i,n_2-3} - 18y_{i,n_2-2} + 10y_{i,n_2-1} + 3y_{i,n_2}\Big) + \mathcal{O}(\Delta\eta^4)$$

Finite difference approximations for the other derivative in the PDE (44) are given by

$$(p_{sc})_{tt} = \frac{1}{\Delta t^2}\Big((p_{sc})_{i,n_2-1}^{n+1} - 2(p_{sc})_{i,n_2-1}^n + (p_{sc})_{i,n_2-1}^{n-1}\Big) + \mathcal{O}(\Delta t^2)$$

$$(p_{sc})_{\xi\xi} = \frac{1}{12}\Big(-(p_{sc})_{i-2,n_2-1}^n + 16(p_{sc})_{i-1,n_2-1}^{-} 30(p_{sc})_{i,n_2-1}^n$$

$$+ 16(p_{sc})_{i+1,n_2-1}^n - (p_{sc})_{i+2,n_2-1}^n\Big) + \mathcal{O}(\Delta\xi^4)$$

$$(p_{sc})_{\eta\eta} = \frac{1}{12}\Big(-(p_{sc})_{i,n_2-4}^n + 4(p_{sc})_{i,n_2-3}^n + 6(p_{sc})_{i,n_2-2}^n$$

$$- 20(p_{sc})_{i,n_2-1}^n + 11(p_{sc})_{i,n_2}^n\Big) + \mathcal{O}(\Delta\eta^4)$$

$$(p_{sc})_{\xi\eta} = \frac{1}{144}\bigg[-\Big((p_{sc})_{i-2,n_2-4}^n - 8(p_{sc})_{i-1,n_2-4}^n + 8(p_{sc})_{i+1,n_2-4}^n - (p_{sc})_{i+2,n_2-4}^n\Big)$$

$$+ 6\Big((p_{sc})_{i-2,n_2-3}^n - 8(p_{sc})_{i-1,n_2-3}^n + 8(p_{sc})_{i+1,n_2-3}^n - (p_{sc})_{i+2,n_2-3}^n\Big)$$

$$- 18\Big((p_{sc})_{i-2,n_2-2}^n - 8(p_{sc})_{i-1,n_2-2}^n + 8(p_{sc})_{i+1,n_2-2}^n - (p_{sc})_{i+2,n_2-2}^n\Big)$$

$$+ 10\Big((p_{sc})_{i-2,n_2-1}^n - 8(p_{sc})_{i-1,n_2-1}^n + 8(p_{sc})_{i+1,n_2-1}^n - (p_{sc})_{i+2,n_2-1}^n\Big)$$

$$+ 3\Big((p_{sc})_{i-2,n_2}^n - 8(p_{sc})_{i-1,n_2}^n + 8(p_{sc})_{i+1,n_2}^n$$

$$- (p_{sc})_{i+2,n_2}^n\Big)\bigg] + \mathcal{O}(\Delta\xi^2\Delta\eta^2).$$

54

After substituting them into the PDE (44) and solving for $(p_{sc})_{n+1}$, we get

$$(p_{sc})_{i,n_2-1}^{n+1} = \left(2 - \frac{5\delta^2\alpha}{2} - \frac{5\delta^2\gamma}{3}\right)(p_{sc})_{i,n_2-1}^n \tag{55}$$
$$+ \delta^2\left(-\frac{5\beta}{36} - \frac{\alpha}{12}\right)(p_{sc})_{i-2,n_2-1}^n + \delta^2\left(\frac{4\alpha}{3} + \frac{10\beta}{9}\right)(p_{sc})_{i-1,n_2-1}^n$$
$$+ \delta^2\left(\frac{4\alpha}{3} - \frac{10\beta}{9}\right)(p_{sc})_{i+1,n_2-1}^n + \delta^2\left(\frac{5\beta}{36} - \frac{\alpha}{12}\right)(p_{sc})_{i+2,n_2-1}^n$$
$$- \frac{\delta^2\beta}{72}\Bigg[- \left((p_{sc})_{i-2,n_2-4}^n - 8(p_{sc})_{i-1,n_2-4}^n + 8(p_{sc})_{i+1,n_2-4}^n - (p_{sc})_{i+2,n_2-4}^n\right)$$
$$+ 6\left((p_{sc})_{i-2,n_2-3}^n - 8(p_{sc})_{i-1,n_2-3}^n + 8(p_{sc})_{i+1,n_2-3}^n - (p_{sc})_{i+2,n_2-3}^n\right)$$
$$- 18\left((p_{sc})_{i-2,n_2-2}^n - 8(p_{sc})_{i-1,n_2-2}^n + 8(p_{sc})_{i+1,n_2-2}^n - (p_{sc})_{i+2,n_2-2}^n\right)$$
$$+ 3\left((p_{sc})_{i-2,n_2}^n - 8(p_{sc})_{i-1,n_2}^n + 8(p_{sc})_{i+1,n_2}^n - (p_{sc})_{i+2,n_2}^n\right)\Bigg]$$
$$+ \frac{\delta^2\gamma}{12}\left(-(p_{sc})_{i,n_2-4}^n + 4(p_{sc})_{i,n_2-3}^n + 6(p_{sc})_{i,n_2-2}^n + 11(p_{sc})_{i,n_2}^n\right)$$
$$- (p_{sc})_{i,n_2-1}^{n-1},$$

for $1 \leq i \leq n_1$ and where $\delta = c\Delta t/J$. Using equation (55) we can compute p_{sc} for the second to last ring. We impose the same continuity conditions along the branch cut as described for the second ring, $j = 2$. We now move our computation to the outermost ring.

For r_∞ which is the last ring, $j = n_2$, Several complications arise. First of all we can only use 5-point schemes approximating the derivatives in the direction of η which take us no further than one point outside of the physical domain. We discretize the radiation condition (49) using such a scheme. We also use such a scheme for $(p_{sc})_{\eta\eta}$ in the discretization of the PDE (44). For every other derivative in the direction of η we use 5-point backwards schemes. This way once the PDE (44) is discretized only one point $(p_{sc})_{i,j+1}^n = (p_{sc})_{i,n_2+1}^n$ is not in the physical domain. This is also true for the discretization of the radiation condition (49). Once again we use 5-point centered

55

schemes for derivatives in the direction of ξ and 3-point centered schemes for the time derivatives. For the scale metric factors α, β and γ we use

$$x_\xi = \frac{1}{12}\Big(x_{i-2,n_2} - 8x_{i-1,n_2} + 8x_{i+1,n_2} - x_{i+2,n_2}\Big) + \mathcal{O}(\Delta\xi^4)$$

$$x_\eta = \frac{1}{12}\Big(3x_{i,n_2-4} - 16x_{i,n_2-3} + 36x_{i,n_2-2} - 48x_{i,n_2-1} + 25x_{i,n_2}\Big) + \mathcal{O}(\Delta\eta^4)$$

$$y_\xi = \frac{1}{12}\Big(y_{i-2,n_2} - 8y_{i-1,n_2} + 8y_{i+1,n_2} - y_{i+2,n_2}\Big) + \mathcal{O}(\Delta\xi^4)$$

$$x_\eta = \frac{1}{12}\Big(3y_{i,n_2-4} - 16y_{i,n_2-3} + 36y_{i,n_2-2} - 48y_{i,n_2-1} + 25y_{i,n_2}\Big) + \mathcal{O}(\Delta\eta^4)$$

We discretize the radiation condition (49) using

$$(p_{sc})_t = \frac{1}{2\Delta t}\Big((p_{sc})^{n+1}_{i,n_2} - (p_{sc})^{n-1}_{i,n_2}\Big) + \mathcal{O}(\Delta t^2)$$

$$(p_{sc})_\xi = \frac{1}{12}\Big((p_{sc})^n_{i-2,n_2} - 8(p_{sc})^n_{i-1,n_2} + 8(p_{sc})^n_{i+1,n_2} - (p_{sc})^n_{i+2,n_2}\Big) + \mathcal{O}(\Delta\xi^4)$$

$$(p_{sc})_\eta = \frac{1}{12}\Big(-(p_{sc})^n_{i,n_2-3} + 6(p_{sc})^n_{i,n_2-2} - 18(p_{sc})^n_{i,n_2-1}$$
$$+ 10(p_{sc})^n_{i,n_2} + 3(p_{sc})^n_{i,n_2+1}\Big) + \mathcal{O}(\Delta\eta^4)$$

Finite difference approximations for the other derivative in the PDE (44) are given

by

$$(p_{sc})_{tt} = \frac{1}{\Delta t^2}\Big((p_{sc})_{i,n_2}^{n+1} - 2(p_{sc})_{i,n_2}^{n} + (p_{sc})_{i,n_2}^{n-1}\Big) + \mathcal{O}(\Delta t^2)$$

$$(p_{sc})_{\xi\xi} = \frac{1}{12}\Big(-(p_{sc})_{i-2,n_2}^{n} + 16(p_{sc})_{i-1,n_2}^{n} - 30(p_{sc})_{i,n_2}^{n}$$
$$+ 16(p_{sc})_{i+1,n_2}^{n} - (p_{sc})_{i+2,n_2}^{n}\Big) + \mathcal{O}(\Delta\xi^4)$$

$$(p_{sc})_{\eta\eta} = \frac{1}{12}\Big(-(p_{sc})_{i,n_2-3}^{n} + 4(p_{sc})_{i,n_2-2}^{n} + 6(p_{sc})_{i,n_2-1}^{n}$$
$$- 20(p_{sc})_{i,n_2}^{n} + 11(p_{sc})_{i,n_2+1}^{n}\Big) + \mathcal{O}(\Delta\eta^4)$$

$$(p_{sc})_{\xi\eta} = \frac{1}{144}\Big[3(p_{sc})_{i-2,n_2-4}^{n} - 16(p_{sc})_{i-2,n_2-3}^{n} + 36(p_{sc})_{i-2,n_2-2}^{n}$$
$$- 48(p_{sc})_{i-2,n_2-1}^{n} + 25(p_{sc})_{i-2,n_2}^{n}) - 24(p_{sc})_{i-1,n_2-4}^{n} + 128(p_{sc})_{i-1,n_2-3}^{n}$$
$$- 288(p_{sc})_{i-1,n_2-2}^{n} + 384(p_{sc})_{i-1,n_2-1}^{n} - 200(p_{sc})_{i-1,n_2}^{n} + 24(p_{sc})_{i+1,n_2-4}^{n}$$
$$- 128(p_{sc})_{i+1,n_2-3}^{n} + 288(p_{sc})_{i+1,n_2-2}^{n} - 384(p_{sc})_{i+1,n_2-1}^{n} + 200(p_{sc})_{i+1,n_2}^{n}$$
$$- 3(p_{sc})_{i+2,n_2-4}^{n} + 16(p_{sc})_{i+2,n_2-3}^{n} - 36(p_{sc})_{i+2,n_2-2}^{n}$$
$$+ 48(p_{sc})_{i+2,n_2-1}^{n} - 25(p_{sc})_{i+2,n_2}^{n}\Big] + \mathcal{O}(\Delta\xi^2\Delta\eta^2),$$

Solving the discretization of the radiation condition (49) for $(p_{sc})_{i,n_2+1}^{n}$ which is the only point outside the physical domain, plugging it into the discretization for the

57

PDE (44) and solving it for $(p_{sc})_{i,n_2}^{n+1}$, we obtain

$$
\begin{aligned}
(p_{sc})_{i,n_2}^{n+1} = \frac{1}{1+\sigma}\Bigg\{ &\left[2 - \delta^2\left(\frac{5\alpha}{2} + \frac{50\gamma}{9} + \frac{11J\gamma}{6\kappa}\right)\right](p_{sc})_{i,n_2}^{n} \\
&+ \delta^2\left(-\frac{\alpha}{12} - \frac{25\beta}{72} - \frac{11\gamma\lambda}{36\kappa}\right)(p_{sc})_{i-2,n_2}^{n} \\
&+ \delta^2\left(\frac{4\alpha}{3} + \frac{25\beta}{9} + \frac{22\gamma\lambda}{9\kappa}\right)(p_{sc})_{i-1,n_2}^{n} \\
&+ \delta^2\left(\frac{4\alpha}{3} - \frac{25\beta}{9} - \frac{22\gamma\lambda}{9\kappa}\right)(p_{sc})_{i+1,n_2}^{n} \\
&+ \delta^2\left(-\frac{\alpha}{12} + \frac{25\beta}{72} + \frac{11\gamma\lambda}{36\kappa}\right)(p_{sc})_{i+2,n_2}^{n} \\
&- \frac{\delta^2\beta}{72}\Big[3(p_{sc})_{i-2,n_2-4}^{n} - 16(p_{sc})_{i-2,n_2-3}^{n} + 36(p_{sc})_{i-2,n_2-2}^{n} - 48(p_{sc})_{i-2,n_2-1}^{n} \\
&- 24(p_{sc})_{i-1,n_2-4}^{n} + 128(p_{sc})_{i-1,n_2-3}^{n} - 288(p_{sc})_{i-1,n_2-2}^{n} + 384(p_{sc})_{i-1,n_2-1}^{n} \\
&+ 24(p_{sc})_{i+1,n_2-4}^{n} - 128(p_{sc})_{i+1,n_2-3}^{n} + 288(p_{sc})_{i+1,n_2-2}^{n} - 384(p_{sc})_{i+1,n_2-1}^{n} \\
&- 3(p_{sc})_{i+2,n_2-4}^{n} + 16(p_{sc})_{i+2,n_2-3}^{n} - 36(p_{sc})_{i+2,n_2-2}^{n} + 48(p_{sc})_{i+2,n_2-1}^{n}\Big] \\
&+ \delta^2\gamma\left(\frac{2}{9}(p_{sc})_{i,n_2-3}^{n} - \frac{3}{2}(p_{sc})_{i,n_2-2}^{n} + 6(p_{sc})_{i,n_2-1}^{n}\right) + (\sigma-1)(p_{sc})_{i,n_2}^{n-1}\Bigg\},
\end{aligned}
\tag{56}
$$

for $1 \leq i \leq n_1$ and where $\delta = c\Delta t/J$ and $\sigma = 11\delta\gamma r_\infty/6\kappa$. Equation (56) does not depend on any points outside the physical domain and can be used to compute p_{sc} along the outermost ring. We impose the same continuity conditions at the branch cut as described for the second ring, $j = 2$.

This completes the computations over the entire domain $i = 1, 2, \ldots, n_1$ and $j = 1, 2, \ldots, n_2$ for one level in time. Levels in time are computed for $n = 1, 2, \ldots$ until the max point-wise difference between 2 successive levels in time fall below a specified tolerance ϵ. This uniform convergence is expressed as

$$
\underset{i,j}{\text{Max}}\Big|\, |(p_{sc})_{i,j}^{n}| - |(p_{sc})_{i,j}^{n-1}|\, \Big| < \epsilon.
\tag{57}
$$

In summary, we use 5-point finite difference schemes to give equations (51)-(56) which

58

are used together as we march in time to approximate the harmonic steady state of the scattered wave p_{sc}.

4.2.1 Results Using 5-Point Scheme
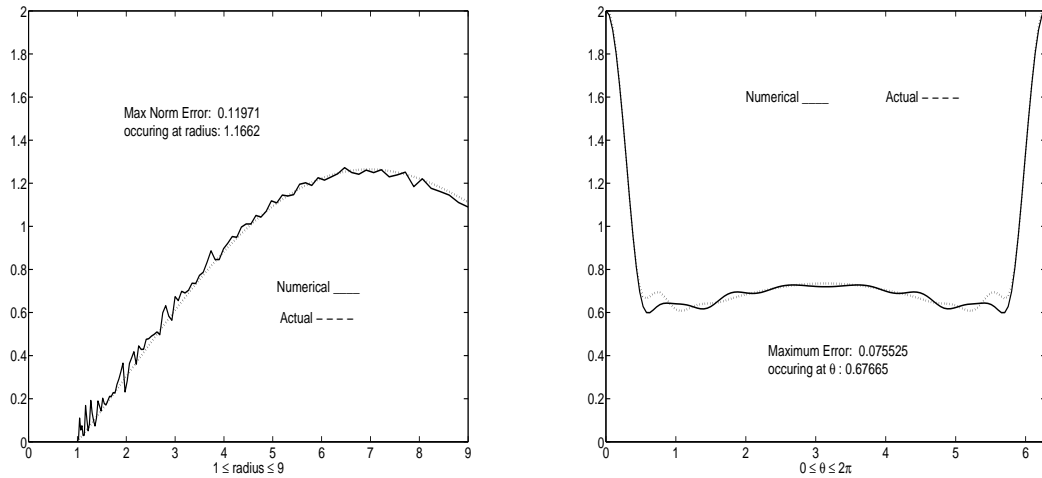
Figure 33: Comparison of Numerical Solution computed on a Winslow grid using the 5-point scheme with 131 rays and 101 rings to Analytical Solution for $\theta = \pi/6$ and Comparison of scattering cross sections

To determine the accuracy of the numerical solution using a higher order 5-point scheme we compare the numerical solution for a circular boundary found using a Winslow grid to the analytical solution. This can only be done for circular boundaries because analytical solutions are not known for boundaries of arbitrary shape. First we set out to determine a grid size which yields desirable results. Grids with too few rays and rings led to inaccurate approximations. As for the 3-point scheme, we don't start to achieve convergence of the numerical solution to the analytical solution until we use grid sizes with around 100 rays and rings. Fig. (33) shows a comparison of the analytical solution to our numerical solution computed on a Winslow grid with 131 rays and 101 rings. The comparison is made along the ray at an angle of $\theta = \pi/6$ from the x-axis. In the same figure is a comparison of the scattering cross section of the

59
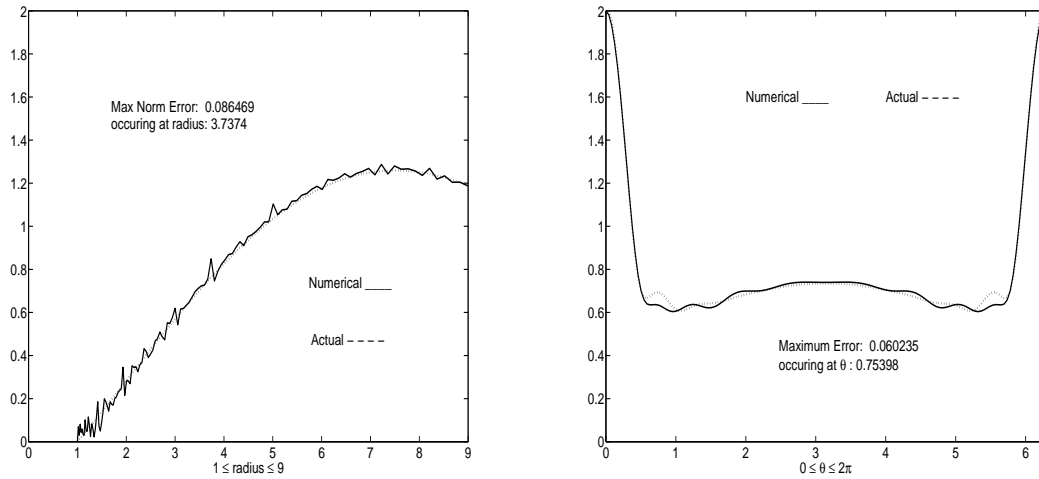
Figure 34: Comparison of Numerical Solution computed on a Winslow grid using the 5-point scheme with 151 rays and 121 rings to Analytical Solution for $\theta = \pi/6$ and Comparison of scattering cross sections
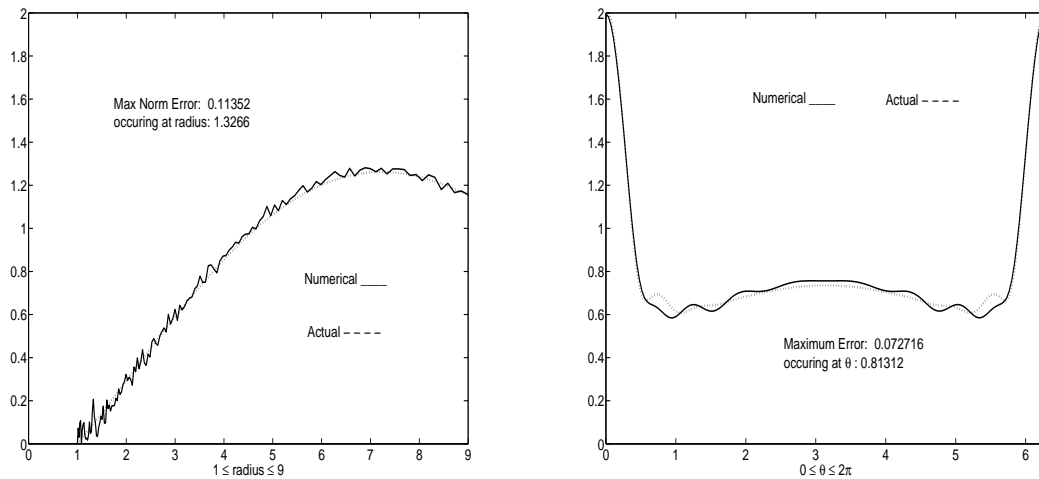
Figure 35: Comparison of Numerical Solution computed on a Winslow grid using the 5-point scheme with 171 rays and 141 rings to Analytical Solution for $\theta = \pi/6$ and Comparison of scattering cross sections

numerical solution against that of the analytical solution. Similar comparisons are made in Fig. (34) and Fig. (35) for grid sizes of 151×121 and 171×141 respectively. It is readily seen that the most accurate grid sizes were 151×121 and 171×141 seen

60

in Fig. (34) and Fig. (35). These should be compared to the 3-point scheme results in Fig. (19) and Fig. (20). The higher 5-point scheme shows a clear improvement especially near the fictitious boundary $r = r_\infty$. The difference between the two grid sizes is negligible and so we favor the smaller 151×121 grid for easier computation. Now that we have narrowed down the selection of appropriate grid sizes for accurate approximations we explore in greater detail and variety the numerical solutions on these grids.

We will vary the step size in time from $\Delta t = 0.0005$ to $\Delta t = 0.05$, and for each step size we will compare the numerical solution to the analytical solution over the entire physical domain. For each step size in time, both the numerical and analytical solutions are computed on the same Winlsow grid and then are compared by taking the absolute value of their point-wise differences. The maximum point-wise differences can be seen in the table in Fig. (36).

rays	rings	Δt	Max Difference with Analytical Solution	Location of Max Difference
151	121	0.0005	0.15052	$(2.0426 , \pm0.8087)$
151	121	0.001	0.14908	$(2.0426 , \pm0.8087)$
151	121	0.005	0.33608	$(1.3159 , 0.0000)$
151	121	0.01	0.31265	$(1.0373 , 0.0000)$
151	121	0.05	no convergence	no convergence

Figure 36: Table comparing the accuracy of the Numerical Solution using the 5-point scheme for varying Δt

The data from the table in Fig. (36) shows that smaller step sizes in time appear to lead to more accurate approximations and that time steps which are too large result in unstable schemes. A comparison between the accuracy of the numerical solution for varying step sizes in time in made in Fig. (37), which shows the 2 plots of the point-wise differences near the obstacle for both $\Delta t = 0.0005$ on the left and $\Delta t = 0.01$ on the right. It is clear that the smaller step size produces a smoother

61
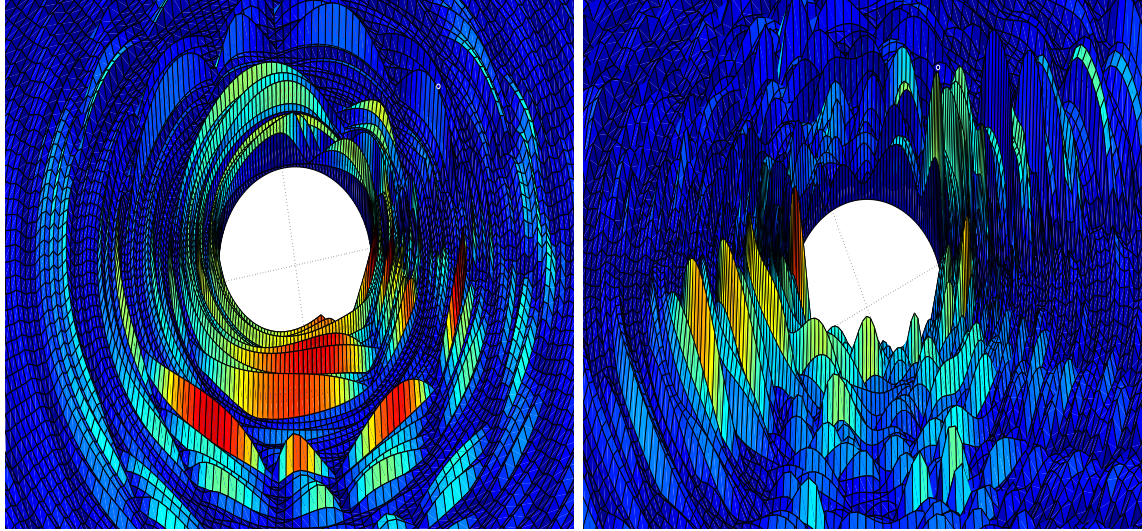
Figure 37: Comparison of plots, near the boundary of the obstacle, of the point-wise differences between the analytical and numerical solutions using the 5-point scheme on a 151×121 Winslow grid with $\Delta t = 0.0005$ on the left and $\Delta t = 0.01$ on the right

and more consistent approximation. This is because of the nature of the Winslow grid. Fig. (10) shows how Winslow grids are irregular in radius step sizes. The rings are tightly clustered near the boundary of the obstacle creating a finer mesh near the obstacle. For accuracy near the obstacle it is necessary to also have smaller step sizes in time. Near the obstacle, the step size of $\Delta t = 0.01$ is too large by comparison to the radius and angle step sizes giving a less smooth result while the step size $\Delta t = 0.05$ was simply too large for convergence. This implies that stability conditions exist but are not known at present. A plot of the numerical solution using a 5-point scheme can be seen in Fig. (38). The average point-wise difference with the analytical solution is 0.024156 which is about a 1% error.

Figure 38: Numerical Solution using a 151×121 Winslow grid with $\Delta t = 0.0005$ and a 5-point scheme

5　Appendix

5.1　Asymptotic Properties of the Hankel functions

Hankel functions are usually written as $H_n^{(i)}(z)$, where $i = 1, 2$. They are defined in terms of the Bessel functions of the first kind and Bessel functions of the second kind. In fact,

$$
\begin{aligned}
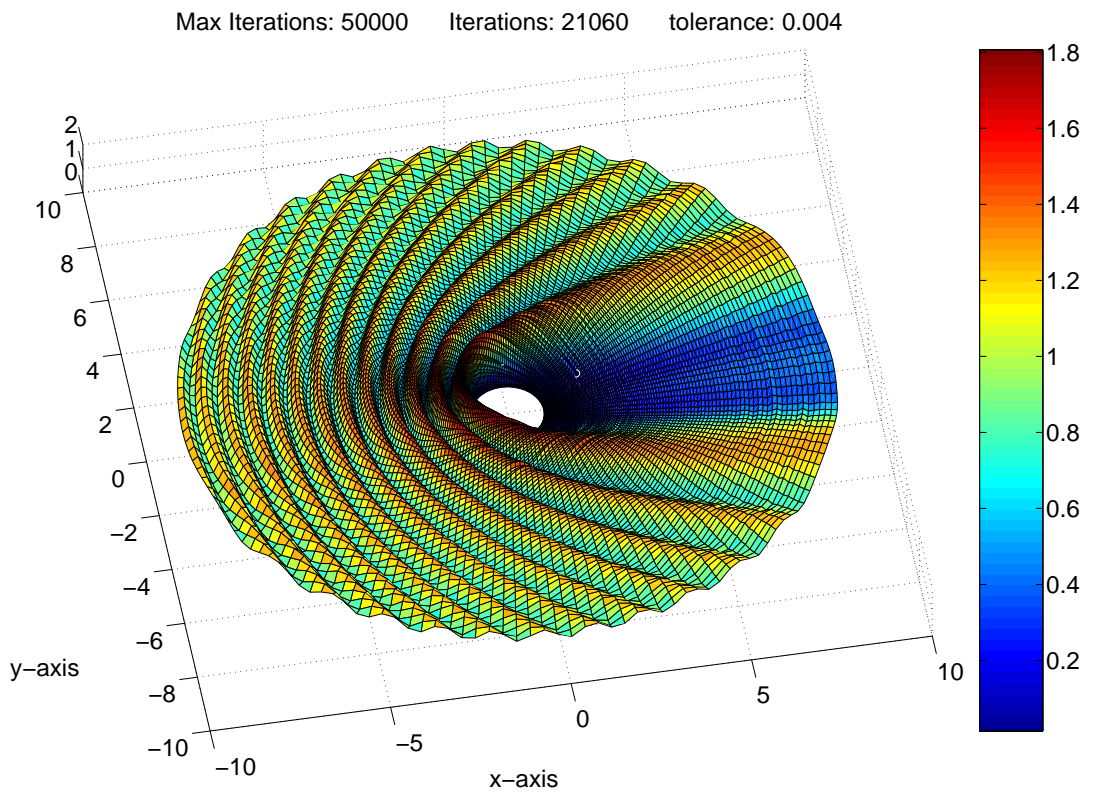H_n^{(1)}(z) &\equiv J_n(z) + iY_n(z), \\
H_n^{(2)}(z) &\equiv J_n(z) - iY_n(z).
\end{aligned}
$$

They have the following asymptotic properties for large z

$$
H_n^{(1)}(z) \sim \sqrt{\frac{2}{\pi z}} e^{i\left(z - \frac{n\pi}{2} - \frac{\pi}{4}\right)}.
$$

In particular,

$$
\begin{aligned}
H_0^{(1)}(z) &\underset{z \longrightarrow \infty}{\longrightarrow} \sqrt{\frac{2}{\pi z}} e^{i\left(z - \frac{\pi}{4}\right)} e^0 &=& \sqrt{\frac{2}{\pi z}} e^{i\left(z - \frac{\pi}{4}\right)} \\
H_1^{(1)}(z) &\underset{z \longrightarrow \infty}{\longrightarrow} \sqrt{\frac{2}{\pi z}} e^{i\left(z - \frac{\pi}{4}\right)} e^{-\frac{\pi}{2}} &=& -i\sqrt{\frac{2}{\pi z}} e^{i\left(z - \frac{\pi}{4}\right)} \\
&\vdots& \\
H_n^{(1)}(z) &\underset{z \longrightarrow \infty}{\longrightarrow} \sqrt{\frac{2}{\pi z}} e^{i\left(z - \frac{\pi}{4}\right)} e^{\left(-\frac{i}{\pi}2\right)^n} &=& (-i)^n \sqrt{\frac{2}{\pi z}} e^{i\left(z - \frac{\pi}{4}\right)}.
\end{aligned}
$$

Analogously, for large z

$$
H_n^{(2)}(z) \sim \sqrt{\frac{2}{\pi z}} e^{-i\left(z - \frac{n\pi}{2} - \frac{\pi}{4}\right)}.
$$

More precisely,

$$
H_n^{(2)}(z) \underset{z \longrightarrow \infty}{\longrightarrow} i^n \sqrt{\frac{2}{\pi z}} e^{i\left(z - \frac{\pi}{4}\right)}, \quad n = 0, 1, 2 \cdots
$$

64

5.2   Improved Radiation Condition: Annihilating Operators

Let's consider the Wilcox [12] expansion (22) of $p_{sc}(r, \theta, t)$ which is a solution to the scattering problem. As $r \to \infty$,

$$p_{sc}(r, \theta, t) \to \omega(r, \theta) \frac{e^{ikr}}{\sqrt{r}} e^{-ikt}, \tag{58}$$

where

$$\omega(r, \theta) \equiv \sum_{n=2}^{\infty} \frac{A_j(\theta)}{r^j}. \tag{59}$$

The operator due to Sommerfeld is

$$R_0 \equiv \frac{\partial}{\partial t} + \frac{\partial}{\partial r} \tag{60}$$

As $r \to \infty$ we apply the operator R_0 to W using (58) and (59) to get

$$
\begin{aligned}
R_0(p_{sc}) = \frac{\partial p_{sc}}{\partial t} + \frac{\partial p_{sc}}{\partial r} &= \left(-ik \frac{\omega}{\sqrt{r}} + ik \frac{\omega}{\sqrt{r}} - \frac{1}{2} \frac{\omega}{r^{3/2}} + \frac{\omega_r}{r^{1/2}} \right) e^{ikr} e^{-ikt} \\
&= \left(-\frac{1}{2} \frac{A_o}{r^{3/2}} - \frac{1}{2} \frac{A_1}{r^{5/2}} + \dots \right. \\
&\qquad \left. - \frac{A_1}{r^{5/2}} - \frac{2A_2}{r^{7/2}} - \dots \right) e^{ikr} e^{-ikt} = O\left(1/r^{3/2}\right),
\end{aligned}
$$

which is of order $O\left(1/r^{3/2}\right)$.

Theorem 2. *The operator*

$$R_1 \equiv \frac{\partial}{\partial t} + \frac{\partial}{\partial r} + \frac{1}{2r}, \tag{61}$$

65

applied to W as $r \to \infty$ gives

$$R_1(p_{sc}) = \frac{\partial p_{sc}}{\partial t} + \frac{\partial p_{sc}}{\partial r} + \frac{p_{sc}}{2r} = O\left(1/r^{5/2}\right), \tag{62}$$

is of order $O\left(1/r^{5/2}\right)$ and can be expressed in terms of Sommerfeld's operator in (60) by

$$R_1(p_{sc}) = \frac{R_0\left[r^{1/2}p_{sc}\right]}{r^{1/2}}. \tag{63}$$

Proof: Using the product rule we have

$$\begin{aligned}
R_0\left(r^{1/2}p_{sc}\right) &= R_0(r^{1/2})p_{sc} + r^{1/2}R_0(p_{sc}) \\
&= \frac{1}{2r^{1/2}}p_{sc} + r^{1/2}R_0(p_{sc}) \\
&= r^{1/2}\left[R_0(p_{sc}) + \frac{1}{2r}(p_{sc})\right]
\end{aligned}$$

Dividing both sides by $r^{1/2}$ gives

$$\frac{R_0\left(r^{1/2}p_{sc}\right)}{r^{1/2}} = R_0(p_{sc}) + \frac{1}{2r}p_{sc} = \frac{\partial p_{sc}}{\partial t} + \frac{\partial p_{sc}}{\partial r} + \frac{p_{sc}}{2r} = R_1(p_{sc})$$

which proves the relationship between R_0 and R_1 in (63). As $r \to \infty$ we use (58) and (59) to get

$$\begin{aligned}
R_1(p_{sc}) = \frac{R_0\left(r^{1/2}p_{sc}\right)}{r^{1/2}} &= \frac{R_0\left(\omega(r,\theta)e^{ikr}e^{-ikt}\right)}{r^{1/2}} \\
&= \left(-ik\omega + ik\omega + \omega_r\right)r^{-1/2}e^{ikr}e^{-ikt} \\
&= \frac{-1}{r^{5/2}}A_1 - \frac{\partial A_2}{r^{7/2}} + \cdots = O\left(1/r^{5/2}\right),
\end{aligned}$$

which is of order $O\left(1/r^{5/2}\right)$ ∎

66

Bayliss [1] established a pattern to construct operators from (63) which have higher orders of convergence as $r \to \infty$. He established

$$R_m(p_{sc}) \equiv \frac{R_0^m(r^{m-1/2}p_{sc})}{r^{m-1/2}} \quad m = 1, 2, \ldots. \tag{64}$$

As $r \to \infty$ the orders of convergence are

$$\frac{R_0^m(r^{m-1/2}p_{sc})}{r^{m-1/2}} = O(1/r^{2m+1/2})$$

We prove it for $m = 2$.

Theorem 3. *As $r \to \infty$ the operator applied to p_{sc} defined by*

$$R_2(p_{sc}) \equiv \frac{R_0^2(r^{3/2}p_{sc})}{r^{3/2}} = O(1/r^{9/2}), \tag{65}$$

is of order $O(1/r^{9/2})$ and is given by

$$R_2(p_{sc}) = (p_{sc})_{tt} + 2(p_{sc})_{tr} + (p_{sc})_{rr} + \frac{3}{r}(p_{sc})_t + \frac{3}{r}(p_{sc})_r + \frac{3}{4r^2}p_{sc}. \tag{66}$$

Proof: As $r \to \infty$ we use (58) and (59) to get

$$\begin{aligned}
\frac{R_0^2\left(r^{3/2}p_{sc}\right)}{r^{3/2}} &= \frac{1}{r^{3/2}}R_0^2\left(r\omega(r,\theta)e^{ikr}e^{-ikt}\right) \\
&= \frac{1}{r^{3/2}}R_0\left(\left(ikr\omega + \omega + r\omega_r - ikr\omega\right)e^{ikr}e^{-ikt}\right) \\
&= \frac{1}{r^{3/2}}\left[2\omega_r + r\omega_{rr}\right]e^{ikr}e^{-ikt} \\
&= \frac{1}{r^{3/2}}\left[2\left(-\frac{A_1}{r^2} - \frac{2A_2}{r^3} + \ldots\right)\right. \\
&\quad \left. + r\left(\frac{2A_1}{r^3} + \frac{6A_2}{r^4} + \ldots\right)\right]e^{ikr}e^{-ikt} = O\left(1/r^{9/2}\right),
\end{aligned}$$

67

which proves the order of convergence. Also we have

$$
\begin{aligned}
\frac{R_0^2\big(r^{3/2}p_{sc}\big)}{r^{3/2}} =& \frac{1}{r^{3/2}}R_0\left(R_0\left(r^{3/2}\right)p_{sc} + r^{3/2}R_0(p_{sc})\right) \\
=& \frac{1}{r^{3/2}}R_0\left(\frac{3}{2}r^{1/2}p_{sc} + r^{3/2}R_0(p_{sc})\right) \\
=& \frac{1}{r^{3/2}}\left(\frac{3}{4}r^{-1/2}p_{sc} + 3r^{1/2}R_0(p_{sc}) + r^{3/2}R_0^2(p_{sc})\right) \\
=& R_0^2(p_{sc}) + \frac{3}{r}R_0(p_{sc}) + \frac{3}{4r^2}p_{sc}.
\end{aligned}
$$

The operator R_0^2 is given by

$$
R_0^2(p_{sc}) = (p_{sc})_{tt} + 2(p_{sc})_{tr} + (p_{sc})_{rr},
$$

which gives

$$
\begin{aligned}
R_2(p_{sc}) =& \frac{R_0^2(r^{3/2}p_{sc})}{r^{3/2}} \\
=& (p_{sc})_{tt} + 2(p_{sc})_{tr} + (p_{sc})_{rr} + \frac{3}{r}(p_{sc})_t + \frac{3}{r}(p_{sc})_r + \frac{3}{4r^2}p_{sc} \ \blacksquare
\end{aligned}
$$

In summary we have the three operators

$$
R_0(p_{sc}) \equiv (p_{sc})_t + (p_{sc})_r = \ O(1\,/\,r^{3/2}) \tag{67}
$$

$$
R_1(p_{sc}) \equiv (p_{sc})_t + (p_{sc})_r + \frac{p_{sc}}{2r} = \ O(1\,/\,r^{5/2}) \tag{68}
$$

$$
R_2(p_{sc}) \equiv (p_{sc})_{tt} + 2(p_{sc})_{tr} + (p_{sc})_{rr} + \frac{3}{r}(p_{sc})_t \tag{69}
$$

$$
+ \frac{3}{r}(p_{sc})_r + \frac{3}{4r^2}p_{sc} = \ O(1\,/\,r^{9/2}).
$$

Operator (67) is the well known Sommerfeld radiation condition. Operator (68) is the

improved operator used in this paper in place of the Sommerfeld radiation condition

68

for numerical solutions of the wave scattering IBVP. Operator (69) has yet to be tested in numerical solutions of the IBVP.

5.3 Wave equation in variables ξ and η

Winslow's Algorithm for grid generation produces a one-to-one transformation $\mathcal{T}$ which maps (ξ, η) from a rectangular computational domain $\mathcal{D}'$ to coordinates (x, y) in a physical domain $\mathcal{D}$.

$$x = x(\xi, \eta) \qquad\qquad y = y(\xi, \eta)$$

The transformation is one-to-one and thus has an inverse transformation $\mathcal{T}^{-1}$ which maps coordinates (x, y) to coordinates (ξ, η).

$$\xi = \xi(x, y) \qquad\qquad \eta = \eta(x, y)$$

The Jacobian matrix of this transformation is given by

$$\widehat{\mathcal{J}} = \begin{bmatrix} \xi_x & \xi_y \\ \eta_x & \eta_y \end{bmatrix},$$

the determinant of which is the Jacobian

$$\hat{J} = \xi_x \eta_y - \xi_y \eta_x.$$

Proposition 2. *If the Jacobian matrix of the transformation* $\mathcal{T} : \mathcal{D}' \to \mathcal{D}$ *is*

$$\mathcal{J} = \begin{bmatrix} x_\xi & x_\eta \\ y_\xi & y_\eta \end{bmatrix},$$

69

then

$$\widehat{\mathcal{J}} = \mathcal{J}^{-1}.$$

Proof: Start with the functions

$$F(x, y) = x - x\Big(\xi(x, y), \eta(x, y)\Big) = 0$$
$$G(x, y) = y - y\Big(\xi(x, y), \eta(x, y)\Big) = 0.$$

Take the partial derivatives with respect to x to get

$$F_x(x, y) = 1 - x_\xi \xi_x - x_\eta \eta_x = 0,$$
$$G_x(x, y) = -y_\xi \xi_x - y_\eta \eta_x = 0.$$

This system of equations in matrix form is

$$\begin{bmatrix} x_\xi & x_\eta \\ y_\xi & y_\eta \end{bmatrix} \begin{bmatrix} \xi_x \\ \eta_x \end{bmatrix} = \begin{bmatrix} 1 \\ 0 \end{bmatrix}. \tag{70}$$

Do the same with the partial derivatives with respect to y to get

$$\begin{bmatrix} x_\xi & x_\eta \\ y_\xi & y_\eta \end{bmatrix} \begin{bmatrix} \xi_y \\ \eta_y \end{bmatrix} = \begin{bmatrix} 0 \\ 1 \end{bmatrix}. \tag{71}$$

Systems (70) and (71) can be combined to be

$$\mathcal{J}\widehat{\mathcal{J}} = \begin{bmatrix} x_\xi & x_\eta \\ y_\xi & y_\eta \end{bmatrix} \begin{bmatrix} \xi_x & \xi_y \\ \eta_x & \eta_y \end{bmatrix} = \begin{bmatrix} 1 & 0 \\ 0 & 1 \end{bmatrix} = I.$$

70

Thus $\widehat{\mathcal{J}} = \mathcal{J}^{-1}$ ∎

The determinant of $\mathcal{J}$ is

$$J = x_\xi y_\eta - x_\eta y_\xi.$$

and so we have

$$\mathcal{J}^{-1} = \frac{1}{J} \begin{bmatrix} y_\eta & -x_\eta \\ -y_\xi & x_\xi \end{bmatrix} = \begin{bmatrix} \xi_x & \xi_y \\ \eta_x & \eta_y \end{bmatrix} = \widehat{\mathcal{J}}. \tag{72}$$

Matching entries in (72) gives

$$\xi_x = \frac{y_\eta}{J} \qquad \eta_x = -\frac{y_\xi}{J} \qquad \xi_y = -\frac{x_\eta}{J} \qquad \eta_y = \frac{x_\xi}{J}. \tag{73}$$

We now look to the wave equation in coordinates x and y in terms of the coordinates ξ and η. Let $W = W\Big(\xi(x,y), \eta(x,y), t\Big)$ and using the equations in (73) we get

$$W_x = W_\xi \xi_x + W_\eta \eta_x = \frac{1}{J}\Big(W_\xi\, y_\eta - W_\eta y_\xi\Big)$$
$$W_y = W_\xi \xi_y + W_\eta \eta_y = \frac{1}{J}\Big(-W_\xi\, x_\eta + W_\eta x_\xi\Big)$$

The second order derivatives yield

$$W_{xx} = W_{\xi\xi}\xi_x^2 + W_{\xi\eta}\eta_x\xi_x + W_\xi\xi_{xx} + W_{\eta\eta}\eta_x^2 + W_{\eta\xi}\xi_x\eta_x + W_\eta\eta_{xx}$$
$$= J^{-2}\Big(W_{\xi\xi}y_\eta^2 - 2W_{\xi\eta}y_\eta y_\xi + W_{\eta\eta}y_\xi^2\Big) + A\,J^{-3}\Big(y_\eta W_\xi - y_\xi W_\eta\Big)$$
$$+ B\,J^{-3}\Big(x_\xi W_\eta - x_\eta W_\xi\Big),$$

71

and

$$W_{yy} = W_{\xi\xi}\xi_y^2 + W_{\xi\eta}\eta_y\xi_y + W_\xi\xi_{yy} + W_{\eta\eta}\eta_y^2 + W_{\eta\xi}\xi_y\eta_y + W_\eta\eta_{yy}$$
$$= J^{-2}\Big(W_{\xi\xi}x_\eta^2 - 2W_{\xi\eta}x_\eta x_\xi + W_{\eta\eta}x_\xi^2\Big) + C\,J^{-3}\Big(y_\eta W_\xi - y_\xi W_\eta\Big)$$
$$+ D\,J^{-3}\Big(x_\xi W_\eta - x_\eta W_\xi\Big),$$

where

$$A = -\Big(x_{\xi\xi}y_\eta^2 - 2x_{\xi\eta}y_\xi y_\eta + x_{\eta\eta}y_\xi^2\Big)$$
$$B = -\Big(y_{\xi\xi}y_\eta^2 - 2y_{\xi\eta}y_\xi y_\eta + y_{\eta\eta}y_\xi^2\Big)$$
$$C = -\Big(x_{\xi\xi}x_\eta^2 - 2x_{\xi\eta}x_\xi x_\eta + x_{\eta\eta}x_\xi^2\Big)$$
$$D = -\Big(y_{\xi\xi}x_\eta^2 - 2y_{\xi\eta}x_\xi x_\eta + y_{\eta\eta}x_\xi^2\Big).$$

The Laplacian is

$$\nabla^2 W(x,y) = W_{xx} + W_{yy}$$
$$= J^{-2}\Big(\alpha W_{\xi\xi} - 2\beta W_{\xi\eta} + \gamma W_{\eta\eta}\Big)$$
$$+ J^{-3}\Big(\alpha x_{\xi\xi} - 2\beta x_{\xi\eta} + \gamma x_{\eta\eta}\Big)\Big(y_\xi W_\eta - y_\eta W_\xi\Big)$$
$$+ J^{-3}\Big(\alpha y_{\xi\xi} - 2\beta y_{\xi\eta} + \gamma y_{\eta\eta}\Big)\Big(x_\eta W_\xi - x_\xi W_\eta\Big),$$

where $\alpha = x_\eta^2 + y_\eta^2$, $\beta = x_\xi x_\eta + y_\xi y_\eta$, and $\gamma = x_\xi^2 + y_\xi^2$ are the metric scale factors and $J = x_\xi y_\eta - x_\eta y_\xi$ is the Jacobian of the transformation $\mathcal{T}$. Thus the wave equation

$W_{tt} = \nabla^2 W(x, y)$ becomes

$$W_{tt} = J^{-2}\Big(\alpha W_{\xi\xi} - 2\beta W_{\xi\eta} + \gamma W_{\eta\eta}\Big) \tag{74}$$
$$+ J^{-3}\Big(\alpha x_{\xi\xi} - 2\beta x_{\xi\eta} + \gamma x_{\eta\eta}\Big)\Big(y_\xi W_\eta - y_\eta W_\xi\Big)$$
$$+ J^{-3}\Big(\alpha y_{\xi\xi} - 2\beta y_{\xi\eta} + \gamma y_{\eta\eta}\Big)\Big(x_\eta W_\xi - x_\xi W_\eta\Big)$$

73

References

[1] A. Bayliss and E. Turkel, Radiation boundary conditions for wave-like equations, *Comm. Pure Appl. Math.* **35**, 707 (1980).

[2] P. Knupp and S. Steinberg, *Fundamentals of Grid Generation* (CRC Press, Boca Raton, FL, 1993).

[3] G.A. Kreigsmann, Exploiting the limiting amplitude principle to numerically solve scattering problems *Wave Motion*, **4**, 371, (1982).

[4] J.F. Thompson, F.C. Thames, and C.W. Matsin, Automatic numerical generation of body-fitting curvilinear coordinate system for field containing any number of arbitrary two-dimensional bodies, *J. Comput. Phys.* **15**, 299, (1974).

[5] A. Winslow, Numerical solution of the quasilinear poisson equations in a nonuniform triangle mesh, *J. Comput. Phys.*, **2**, 149, (1967).

[6] V. Villamizar and O. Rojas, Time-dependent numerical method with boundary-conforming curvilinear coordinates applied to wave interactions with prototypical antennas, *J. Comput. Phys.*, **177**, 1-36, (2002).

[7] V. Villamizar and R. Jimenez, Scattering cross section of a cylinder at the interface of two acoustic media, *in Proc. 4th Int. Conf. Mathematical and Numerical Aspects of Wave Propogation Phenomena, Colorado, 1998,* edited by J.A. DeSanto (SIAM, Philadephia, 1998), p. 641.

[8] A. Taflove and S.C. Hagness, *Computational Electrodynamics. The Finite-Difference Time-Domain Method, 2nd ed.*(Artech House, Norwood, MA, 2000).

[9] J.F. Thompson. Elliptic grid generation. In J.F. Thompson, editor, *Numerical Grid Generation. Proceedings of a Symposium on the Numerical Generation*

of Curvilinear Coordinate Systems and their Use in the Numerical Solution of PDE's, pages 79-105, Tennessee, 1982. North-Holland.

[10] A.N. Tikhonov and A.A. Samarskii. *Equations of Mathematical Physics*, Dover Publications, New York, 1963.

[11] J.W Thomas. *Numerical Partial Differential Equations, Finite Difference Methods*, Springer Publications, New York, 1995.

[12] C.H. Wilcox. An expansion theorem for electromagnetic fields, *Comm. Pure Appl. Math.* 9, 115-134 (1956).

[13] A.A. Amsden and C.W. Hirt. *A simple scheme for generating general curvilinear grids* , J. Comp. Phys., 98, (1973) 348-349.

[14] P.M. Morse and K.U. Ingard. *Theoretical Acoustics* (McGraw-Hill Book Co., New York, 1968), pp.332-338. Reprinted by Princeton University Press, Princeton, NJ, 1986.